ADVANCED ENGINEERING MATERIALS
www.aem-journal.com

Microstructural, Mechanical, and Tribological Characterization of Selective Laser Melted CoCrMo Alloy under Different Heat Treatment Conditions and Hot Isostatic Pressing

Giovanna Cornacchia, Silvia Cecchel, Davide Battini, Candida Petrogalli, and Andrea Avanzini*

A deep knowledge of material properties is fundamental to obtain high-performance medical implants realized with CoCrMo alloy manufactured by selective laser melting (SLM), even more so when considering that heat treatments (HTs) are often necessary to refine the microstructure, eliminate residual stress, and improve mechanical properties. To this aim, herein, SLM CoCrMo alloy samples are produced in six different treatment conditions: as built (AB), four different vacuum HTs, and hot isostatic pressing (HIP). Modifications to microstructure, hardness, tensile behavior, and wear resistance are then investigated. Results reveal that vacuum HTs and HIP have different effects on microstructure and types of defects with respect to the AB condition. Thus, proper selection of the treatment is mandatory to improve specific mechanical properties, such as strength, ductility, hardness, or tribological response. In this context, it is confirmed that the choice of an appropriate HT allows SLM CoCrMo to reach the target mechanical properties set by international standards for applications in the medical field, such as dentistry or orthopedics.

1. Introduction

Cobalt–Chromium (Co–Cr) alloys provide one the best balance between mechanical strength, durability, and wear, associated with good corrosion resistance and biocompatibility.[1] Traditional processing routes of Co–Cr alloys include investment casting, hot forging and subtractive processes (computer aided design (CAD)/computer aided manufacturing (CAM) milling). Investment casting allows the manufacturing of devices with complex shapes but usually low mechanical properties due to the presence of solidification defects, large grains, and inhomogeneous microstructure. Forged constructions exhibit improved properties, but typical disadvantages are higher cost and a reduced flexibility on geometry.

Recently, additive manufacturing (AM)[2] emerged as an alternative technology which could provide an optimal trade-off between conflicting requirements or even pave the way to new applications, in particular for the biomedical industry. In the orthopedic field, examples include manufacturing of a dense femoral component[3] or investigations on cellular structures,[4,5] demonstrating that controlling material porosity can lead to a better stress transfer to the peri-implant area, thanks to stiffnesses that match favorably with bone structures. In dentistry, potential applications include components of removable partial denture (RPD), such as clasp retainer,[6] or fixed dental prosthesis (i.e., metal ceramic restoration).[7] Considering masticatory actions, key requirements for dental devices are high strength and resilience, high stiffness, and elongation at break[8] to withstand biting forces without fracture. The possibility of using AM for cardiovascular Co–Cr stents by selective laser melting (SLM) was also preliminarily explored.[9] In the orthopedic field, load bearing components have to comply with strict strength requirements but, they should also ideally guarantee optimal stiffness to reduce stress-shielding effects in prostheses. Sliding parts, such as the components of artificial joints, must ensure excellent tribological performances, minimizing wear debris generation from the worn surfaces, which can otherwise trigger a cascade of adverse tissue responses.[10] Thus, it is clear that a remarkable versatility is required for the material to cope with structural and functional requirements that might even be contrasting due to the aforementioned dissimilarities of biomedical components.

For these purposes, the material properties and potential failure modes must be deeply investigated to preserve the safety and performance levels required by the biomedical industry.

G. Cornacchia, D. Battini, C. Petrogalli, A. Avanzini
Department of Mechanical and Industrial Engineering
University of Brescia
via Branze 38, 25123 Brescia, Italy
E-mail: giovanna.cornacchia@unibs.it

S. Cecchel
Research and development department of Streparava SpA company
Streparava SpA
Via Zocco 13, 25030 Adro (BS), Italy

The ORCID identification number(s) for the author(s) of this article can be found under https://doi.org/10.1002/adem.202100928.

DOI: 10.1002/adem.202100928

Mechanical properties are strictly related to the underlying microstructure which in turn depends on the processing route, as shown in the study by Kim et al.,[11] where a comparison of Co−Cr dental alloys fabricated by different processing methods is reported. In particular, parts processed using SLM technology usually undergo rapid melting and solidification and the grain size is typically much smaller than that of cast parts.

Traditional, CoCrMo alloys are composed of γ (face-centered cubic [FCC] structure) and ε (hexagonal close-packed [HCP] structure) phases which are stable at high and low temperatures, respectively. In the case of SLM CoCrMo, the phases are still γ and ε but their distribution and presence are modified because of the processing technology. Fine-grain strengthening results in higher tensile and yield strengths with respect to cast parts, although processing parameters, such as laser power or scanning speed and pitch, may significantly alter both properties.[12] Heat treatments (HT) may provide an effective way to optimize mechanical properties against specific targets. There exists a large body of literature concerning alloying and thermomechanical treatments used to modify the mechanical strength and ductility of forged or cast Co–Cr alloys[13–17] for complying with international standards such as ASTM F75 or ISO 22674. This aspect has also been the object of a few recent investigations for SLM CoCrMo, although an optimal strategy has not yet been identified. More specifically, Hitzler et al.[18] investigated the properties of laser-melted Co–Cr alloys after stress relief at 800 °C for 20 min or HT at 1150 °C for 1 h in argon atmosphere. In the as-built (AB) condition with stress relief only, the alloys displayed reduced Young's modulus (i.e., below clinical requirements set out in the standard ISO 22674), whereas the HT improved stiffness as well as ductility, strength, and isotropic characteristics. Zhang et al.[19] reported an investigation on the proper combinations of HT temperatures and durations to reach tensile strength, yield strength, and elongation higher than what is required by the ASTM F75. More specifically, they considered corrosion and mechanical properties of SLM CoCrMo after annealing at 1200 °C, followed by different cooling strategies. Particularly, fracture mechanisms were reported to be either ductile or brittle depending on HT. In the work of Song et al.,[20] the material was heated for 2 h at 1200 °C under a nitrogen-protected atmosphere, followed by furnace cooling. This HT caused an increase in the tensile strength and elongation at break of the SLM fabricated parts, reduced yield strength and hardness, and transformed the failure fracture from brittle to slightly ductile. Finally, in the study by Kajima et al.,[21] the microstructures and mechanical properties of CoCrMo alloy specimens fabricated by SLM were studied before and after 6 h of HTs conducted at a temperature ranging from 750 to 1150 °C. It was found that increasing the HT temperature enhanced the ductility of the alloy specimens and decreased their 0.2% yield strength and Vickers hardness values.

Considering tribology and wear properties, the review of the existing literature on metals additively manufactured by laser powder bed fusion (LPBF)[22] reports stainless steel, titanium, aluminum, and nickel alloys, while not including Co–Cr systems. The general conclusion of this survey was that the metallic alloy by LPBF has higher wear resistance and lower coefficient of friction (COF) than metallic alloys produced by traditional processes, mainly due to fine grains and high hardness. Further improvement of the tribological behavior may be achieved by means of surface treatments, as reported in the study by AlMangour et al.,[23] where an increase in wear resistance after shot peening of a DMLS 17-PH4 steel was obtained and attributed to the formation of a strong fine surface layer (i.e., grain refinement) and work-hardening effect.

However, the LPBF processing parameters are fundamental for wear rate (WR) as a fully densified part usually has higher wear resistance and COF. The presence of pores reduces the bonding between molten pools, resulting in cracks. These cracks can further cause material damage which greatly increases wear.

In terms of the relationship between microstructure and tribological properties, some works also considered the possibility of improving wear resistance by directly tuning the laser processing parameters and avoiding the need of post-treatments. As proposed in the study by AlMangour et al.,[24] a careful selection of an optimum processing window could ensure a refined microstructure with adequate densification, allowing to achieve the best tribological properties under harsh wear conditions. In the study by Yang et al.,[25] it was instead suggested that wear resistance can be enhanced by controlling heat flow in SLM to rotate grains away from the "soft" orientation, where grains have low resistance to slip, by means of a combination of scanning strategies and small hatch spacing. For AM CoCr alloys, these approaches are not yet reported, and actually, most of recent literature on the tribology of SLM deals with additively manufactured titanium alloys, due to their special relevance as biomaterials.[26,27]

Considering CoCrMo and its biomedical applications, the main concerns are the formation of wear debris and ion elution, especially for metal-on-metal-type hip replacements. For conventional manufacturing techniques, these seem to be closely related to the microstructure, which is influenced by the γ-to-ε phase transformation and precipitation of intermetallic compounds and carbonitrides.

For SLM CoCrMo at present, the number of papers considering tribology is indeed limited. Duran et al.[28] proposed a comparative tribological characterization of cast and SLM CoCrMo alloys under dry and wet conditions. Under dry sliding, the SLM processed alloy exhibited a superior wear performance against the alumina-based counterpart material, which was attributed to Co-rich matrix being harder for SLM than cast alloy due to its extremely fine microstructure. Under wet conditions (artificial saliva), the SLM layered structure suffered from wear due to formation of microcracks under loading.

In the study by Atapek et al.,[29] the tribocorrosion behavior of CoCrMo alloy produced by casting was compared with the one produced by SLM, using artificial saliva solution and a "ball-on-disc"-type tribometer. It was concluded that the SLM processed alloy was more resistant to both corrosion and wear, thanks to the more homogeneous microstructure, the higher hardness, and the more stable oxide layer formed on the surface.

Although HTs were reported to reduce the wear resistance of several SLM metallic alloys,[22] by changing the microstructure of metallic alloys by LPBF and losing the pretreatment of very fine microstructure, current researches in this field for CoCrMo alloys are extremely limited. In fact, to the authors' knowledge, the only investigation concerning CoCrMo alloys manufactured with the LPBF method is reported in the study by Mantrala et al.[30] The influence of HT on wear performances for CoCrMo alloy was evaluated on samples fabricated using

laser-engineered net shaping (LENS), solutionized at 1200 °C and water quenched. Aging treatment was done at 815 and 830 °C for 2, 4, and 6 h. Overall, the HT improved properties of the laser-fabricated CoCrMo alloy. In particular, the samples solutionized at 1200 °C for 45 min followed by aging at 830 °C for 2 h exhibited highest hardness, whereas the most significant improvement in wear resistance was reported for solutionizing treatment at 1200 °C for 60 min with 4 h aging at 830 °C.

While researches reported in literature highlight the significant influence of HT on the behavior of SLM CoCrMo alloys, the current knowledge remains largely incomplete and no HT strategy has been studied while considering mechanical behavior potential drawbacks on the tribological side and vice versa. To the best of authors' knowledge, no previous research has been published yet, concerning the relationship between tribological behavior and HT conditions or on the possibility to identify the best trade-off between different requirements. Furthermore, hot isostatic pressing (HIP) is often considered as the most effective post-manufacturing treatment through the homogenization and densification of the microstructure achievable thanks to the combined action of high pressure and temperature. In this context, the aim of this work is to extend the knowledge on the aforementioned aspects by comparing the microstructural, mechanical, and tribological performances of AB SLM CoCrMo with respect to HT at different temperatures and times and HIP.

2. Experimental Section

2.1. Samples Description

Morphological and dimensional characterization of the powder used for the AM process was conducted by scanning electron microscopy.

Dogbone-shaped specimens with dimension of 75 × 15 × 3 mm and a gauge length of 5 × 15 mm (**Figure 1**) were produced with Co28Cr6Mo commercial powder from LaserForm by SLM with a ProX DMP 100 system. The nominal composition of the powder is shown in **Table 1**. The specimens were fabricated using a "chessboard" scan strategy, with hatching distance of 10 μm under a laser power of 50 W. The SLM instrument was operated using the standard deposition parameters for ProX DMP 100 system in argon atmosphere. The dumbbell specimens were vertically built on a stainless steel base plate with the building direction parallel to the tensile one (angle of 0° between the building and longitudinal direction). To investigate the real condition on an AM component obtained by DMLS/SLM, the samples surface was not machined, with a surface roughness of $R_a = 10–20$ μm; only the supporting structures were mechanically removed before the tests.

The HIP treatment was conducted at the Bodycote plant of Magny Cours (France), whereas the HTs on samples were conducted by the company TAV Vacuum Furnaces (Caravaggio (BG), Italy), using a horizontal furnace for vacuum HT. To avoid any type of contamination and ensure temperature uniformity, the samples were placed on alumina plates and covered with a metal ring. In particular, all HTs were conducted under high vacuum (10^{-6} mbar) with a "TAV H3 all metal" furnace.

Three samples for each of the six following conditions were analyzed: AB, HT at 800 °C for 20 min, (recommended for dental devices), HT at 800 °C for 2 h, HT at 1150 °C for 2 h, HT at 1150 °C for 6 h, and HIP at 1200 °C for 4 h.

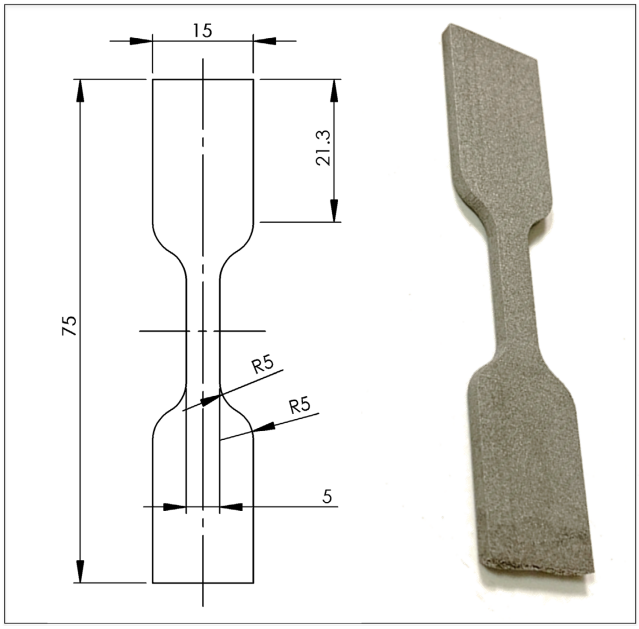

Figure 1. Example of dogbone specimen with its geometry.

Table 1. Chemical composition (wt%) of the commercial laser form Co28Cr6Mo powder.

	Cr	Mo	Si	Mn	Fe	C	Co
Co28Cr6Mo	28–30	5.0–6.0	0.0–1.0	0.0–1.0	0.0–0.50	0.0–0.02	Balance

The selection of HT parameters, after a careful study of the literature, was aimed at obtaining similar mechanical properties to those obtained for conventional alloy in compliance with current standards. In particular, at least one of the five types of the criteria in ISO 22674 must be satisfied to make SLM technology suitable for biomedical devices.

In addition, the selected parameters allowed to compare the results obtained with vacuum and HIP treatments with some of the most interesting works in literature.[14–17]

Table 2 shows the principal parameters of the examined HTs. Before each thermal treatment, the samples underwent a high vacuum cycle at room temperature in the oven to eliminate any contaminants and gases that may be present in the chamber or in the samples.

2.2. Microstructural Observation and Analysis

To analyze microstructures and defects, the different samples were examined using a Leica DMI 5000M optical microscope and LEO EVO-40 XVP scanning electron microscope (SEM) equipped with an energy-dispersive spectrometer (EDS). The porosities were examined with micrographic observations using LAS 4.0 software integrated with the optical microscope. For metallographic investigations, transversal and longitudinal sections of each sample were prepared with standard metallographic

Table 2. Scheme of HT parameters used.

HT	Thermal ramp	Cooling
1150 °C × 2 h	Heating to 950 °C (10 °C min^{-1}) with 1 mbar of partial pressure (Pp) of Ar for 90 min Heating from 950 °C (10 °C min^{-1}) to 1150° with 1 mbar of Pp of Ar for 120 min	Radial cooling from 1150 °C to room temperature (RT) with 3 bars of Ar, with cooling rate of 265 °C min^{-1}, monitored with a thermocouple.
1150 °C × 6 h	Heating to 950 °C (10 °C min^{-1}) with 1 mbar of Pp of Ar for 90 min Heating from 950 °C (10 °C min^{-1}) to 1150° with 1 mbar of Pp of Ar for 360 min	Radial cooling from 1150 °C to RT with 3 bars of Ar, with cooling rate of 265 °C min^{-1}, monitored with a thermocouple.
800 °C × 20 min	Heating to 800 °C (10 °C min^{-1}) with 1 mbar of Pp of Ar for 20 min	Radial cooling from 800 °C to RT with 3 bars of Ar, with cooling rate of 265 °C min^{-1}, monitored with a thermocouple.
800 °C × 2 h	Heating to 800 °C (10 °C min^{-1}) with 1 mbar of Pp of Ar for 120 min	Radial cooling from 800 °C to RT with 3 bars of Ar, with cooling rate of 265 °C min^{-1}, monitored with a thermocouple.
HIP	Heating to 1200 °C for 240 min with 1020 bar in a shared cycle in argon environment.	Slow cooling in the furnace below argon, with cooling rate around 300–400 °C h depending on the load.

techniques (ground with SiC papers and polished with 1 μm diamond paste). The sections were cut off from the shoulders of the tensile specimens before testing. Finally, to better investigate defects and microstructures, the samples were etched with an electrolytic reagent of 5 ml HCl and 10 g $FeCl_3$ in 100 ml of water at 6 V for few seconds, according to ASTM E407 standard. Image analysis was conducted with the software Image J to estimate the phase distribution before and after post-treatments. It should be noted that this approach can lead to slightly inaccurate phase distribution absolute values. However, γ and ε phases' volume fraction estimates can be used for comparative purposes between the AB and the different treatment conditions.

2.3. Hardness and Tensile Test

Vickers microhardness measurements on the etched surfaces before and after HTs were carried out with a Micro Duromat 4000 Reichert Jung instrument, according to ASTM E92-16, using a 9.8 N (1 Kgf) load applied for 15 s. Results are presented as average values of at least ten measurements.

Tensile testing to assess Young's modulus (E), 0.2% yield strength ($R_{p0.2}$), ultimate tensile strength (R_m), and elongation at failure (A%) was conducted at room temperature on three samples for each condition, following UNI EN ISO 6892-1:2009. An electromechanical testing machine Instron 3369 at a strain rate of 1 mm min^{-1} was used for tensile testing. Finally, the tensile fracture surfaces were examined using SEM using a secondary electron (SE) detector.

2.4. Wear Measurements

Pin-on-disk tests were conducted in dry conditions on the samples according to ASTM G99-17 standard using a THT High Temperature Tribometer in the reciprocating sliding configuration. The samples were polished with grinding paper to reach a surface roughness R_a lower than 0.8 μm. An Al_2O_3 ball of 6 mm diameter was used as counterbody under a normal load of 5 N and for a sliding distance of 50 m. COF was recorded during the test and the wear track profile was measured through a stylus profilometer Mitutoyo SJ301 at the end of the test. This step allowed calculating the specific WR using the following equation.

$$\mathrm{WR} = \frac{V}{P*l} \tag{1}$$

where V is the volume loss during the test, while P and l are the normal load and the sliding distance imposed. The wear tracks were also observed using SEM to better understand the wear mechanism.

3. Results and Discussion

3.1. Microstructural Observation

Co28Cr6Mo powder (LaserForm) used in this study was commercially procured and gas atomized. **Figure 2** shows the typical morphology of powders using a scanning electron microscope (SEM) (LEO EVO-40 XVP) integrated with an EDS. As shown, the majority of these powders exhibit spherical shapes. In particular, standards UNI EN ISO 643 and ASTM E112 have been adopted for the dimensional classification of spherical particles. These particles were classified in three groups (small, medium, and large size), as shown in Figure 2. The particle size ranges from 1.95 to 6.9 μm, values close to the medium-particle class. The chemical composition was also verified, confirming the commercial Laser Form Co28Cr6Mo powder shown in Table 1.

The ultimate properties of a component depend on its microstructural features and the microstructure of SLM parts depends primarily on the thermal history, more specifically, on the thermal gradients and cooling rates during manufacturing processing and heat treatments.

In this study, optical microscopy integrated with LAS software was used to study the porosity density, circularity of pores, and microstructures of SLM Co28Cr6Mo. In particular, the fraction of the surface voids over the total surface (average porosity) and circularity were measured from cross-section images. The porosity level strongly depends on the thermal history during laser fabrication, which causes highly dynamic spatial and temporal temperature fields (i.e., concentrated gradients and high heating/cooling speeds) near the melting pool. As a consequence, there is not enough time for conductive homogenization and partially molten particles may cause defects such as pores or inclusions.[31,32]

In **Figure 3**, the presence of different types of pores is highlighted, that can be classified into regular and irregular

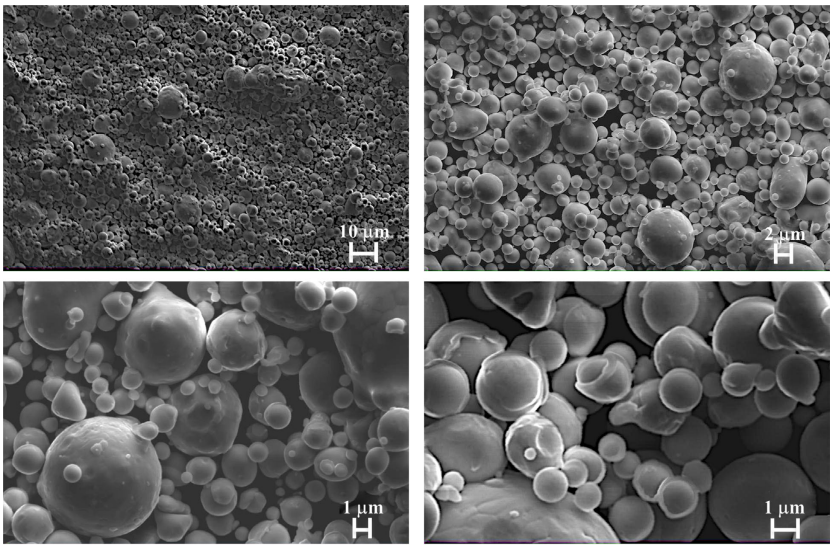

Interval of dimension	1.1÷23.8 μm
Total size average	1.95÷6.9 μm
Average size of large particles	1.91÷12 μm
Average size of medium particles	1.45÷5.8 μm
Average size of small particles	1.45÷2.8 μm

Figure 2. Examples of scanning electron microscopy images of CrCoMo alloy powders at different magnifications with the results of measurements (average and standard deviation).

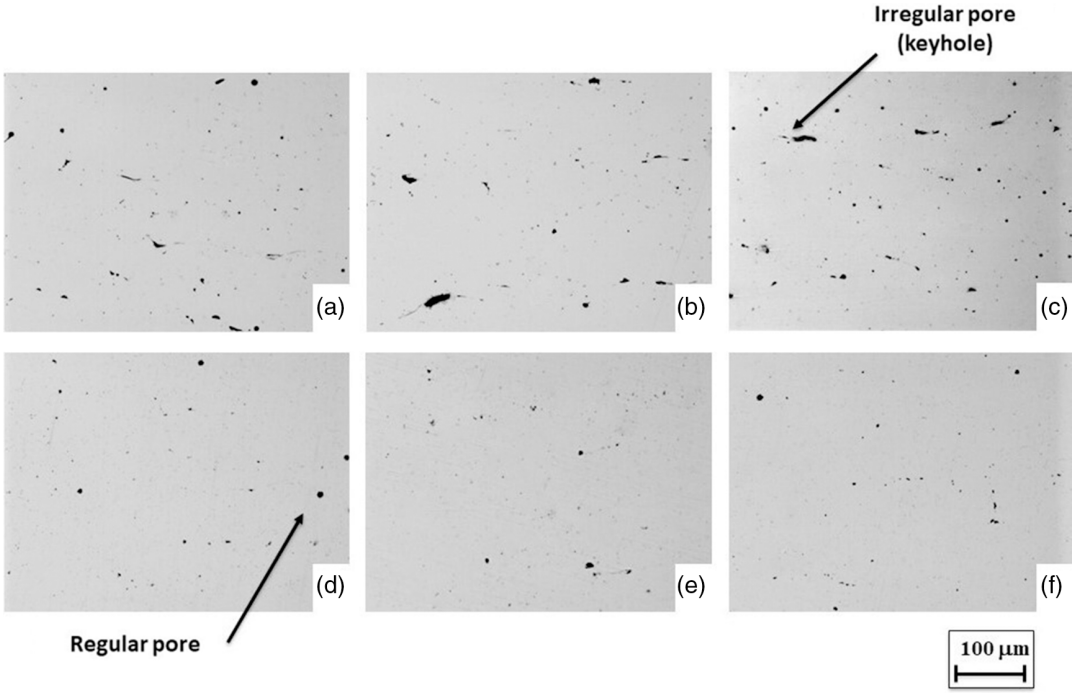

Figure 3. Examples of transversal section of a) AB, b) HT 800 °C for 20 min, c) HT 800 °C for 2 h, d) HT 1150 °C for 2 h, e) HT 1150 °C for 6 h, and f) HIP samples at 200× magnification, in which porosities are visible.

shapes, randomly distributed in each cross section, according with literature.[33–37]

Metallurgical pores, which are formed during the densification process in the final stage of sintering, are due to the entrapments of initial gas retained by the powder bed particles (Ar or N_2) generated from the melt pool, and their shape is small and spherical. The irregular pores (also known as keyhole pores), which are formed during the compacting process, are larger in size and their instability is due to laser−material interaction or inadequate powder melting (i.e., incorrect powder deposition, unexpected changes in powder environment, or geometry) that causes an irregular shape. Local vaporization of alloy elements is instead due to the extremely rapid solidification, and the gas formed during the process can be entrapped in the liquid metal.[38,39]

Studying porosities geometry and distribution is very important because they can strongly influence the alloy mechanical properties by serving as crack initiation sites. In fact, irregular pores usually result in higher local stress concentration than spherical ones.[40–42]

Consequently, as briefly mentioned before, regularity of the voids was measured through the circularity parameter, calculated with LAS 4.0 software. In this context, it is convenient to have a parameter for describing these differences, the equivalent diameter and the shape factor being among the most used. A threshold value of 1.5 was assumed to distinguish between regular (circularity ≤ 1.5) and irregular pores (circularity > 1.5). The total porosity quantity was instead evaluated as the total porosity area over the section area (expressed in percent) on many micrographs for each treatment condition.

Table 3 shows the difference in terms of porosity measurements obtained for AB and heat-treated samples.

This analysis allows to highlight the difference between AB samples and after HT/HIPed ones, both considering percentage or shape parameter of porosity. An interesting work of AlMangour et al.[43] demonstrated that the HIP process removed most of the internal and interconnected pores; however, the fine porosity still present in some samples might be due to incomplete melting of the powders at the laser track interfaces during the SLM process. The porosity ratio of AB samples of AlMangour et al.[43] is aligned with the observations made on the samples of this research work. It can be noticed that with HIP treatment, the lowest porosity value was achieved, a factor that is considered beneficial both for static mechanical properties and for fatigue behavior because the possible crack nucleation sites decrease.[44] Moreover, the porosity reduction is fundamental also to limiting the risk that, after machining operations, defects turn into superficial irregularities, with a detrimental effect for tribological applications.

Table 3. Mean and standard deviation for porosity area over micrograph area and regular/irregular shape distribution for each condition.

Sample	Mean porosity		Regular pores' quantity	Irregular pores' quantity
	Mean	Std. Dev.		
AB	1.25%	1.08%	88.60%	11.40%
HT 800 °C for 20 min	2.23%	1.95%	89.40%	10.60%
HT 800 °C for 2 h	2.25%	2.48%	91.30%	8.70%
HT 1150 °C for 2 h	0.80%	0.80%	80.20%	19.80%
HT 1150 °C for 6 h	0.92%	0.66%	73.80%	26.20%
HIP	0.54%	0.27%	65.10%	34.90%

Considering the literature, it may be presumed that the influence of HT conditions is due to changes in the grain structure and metallurgical bonding of the particles.[45]

For HT at 1150 °C, a reduction in porosity could be observed, thanks to microstructural rearrangements and the high quality of the treatment under vacuum. On the contrary, treatments at lower temperature resulted in an increase in both the mean and the standard deviation of porosity area over the micrograph area, indicating not only a more porous material but also a more irregular distribution of the pores. The higher quantity of pores for HT at 800 °C could be due to a greater amount of gas trapped within porosity that during vacuum heating expanded, and, in the absence of recrystallization, the porosity increased. In fact, microstructural variations like recrystallization and grain growth, during sinterization or HTs, permit the densification and the removal or shrinkage of the pores.[41] This could also be confirmed by the shape distribution as densification and pore shrinkage cause a partial pore closure, transforming a bigger regular-shaped pore into a smaller irregular-shaped pore.

In general, the porosities found in the samples fall within an acceptable range for SLM products and the regular shape was predominant. An even stronger reduction of regular-shaped defects was found for HIP treatment, possibly due to the consequence of porosity flattening effect due to applied pressure.

HTs and HIP had a substantial impact on microstructure. Optical micrographs of AB samples are shown in **Figure 4**, whereas heat-treated and HIP micrographs are shown in **Figure 5** and **6**, in the longitudinal and transversal sections, respectively. **Figure 7** shows the SEM microstructures of SLM CoCrMo in the longitudinal sections in all conditions. A comparison of the six examined conditions allows understanding the microstructure evolution between the AB condition and the different post-treatments investigated.

A clear example of the typical appearance at an optical microscope for parallel and transverse sections with respect to building direction for AB samples is shown in Figure 4. Arc-shaped molten pool boundaries are found on the longitudinal section, whereas elongated molten boundaries are observed in transversal ones with a distance of about 70 μm, corresponding to the hatching distance. It is possible to note that in the AB condition the stacking scheme of the single-weld beads dominates the micrographs and the transversal section shows a columnar structure along the hatching line, where the boundaries may correspond to the fusion ones formed by laser scan.

According to the literature,[18,46,47] CoCrMo alloys at room temperature present a biphasic structure composed of HCP (ε) and FCC (γ). Observing the phase diagram, the ε phase is the low-temperature phase and it exists as an equilibrium phase at room temperature. It is characterized by plate-like striations and it is known to enhance strength and wear resistance but leads to low elongation. The γ phase is the high-temperature stable phase and shows higher elongation. It is important to highlight that FCC-to-HCP transformation rarely occurs under normal cooling conditions, but it can be thermally encouraged by quenching from 950 to 650 °C or through plastic strain. For this reason, a rapid solidification in the SLM process inhibits martensite formation as the alloys remain in the martensite field

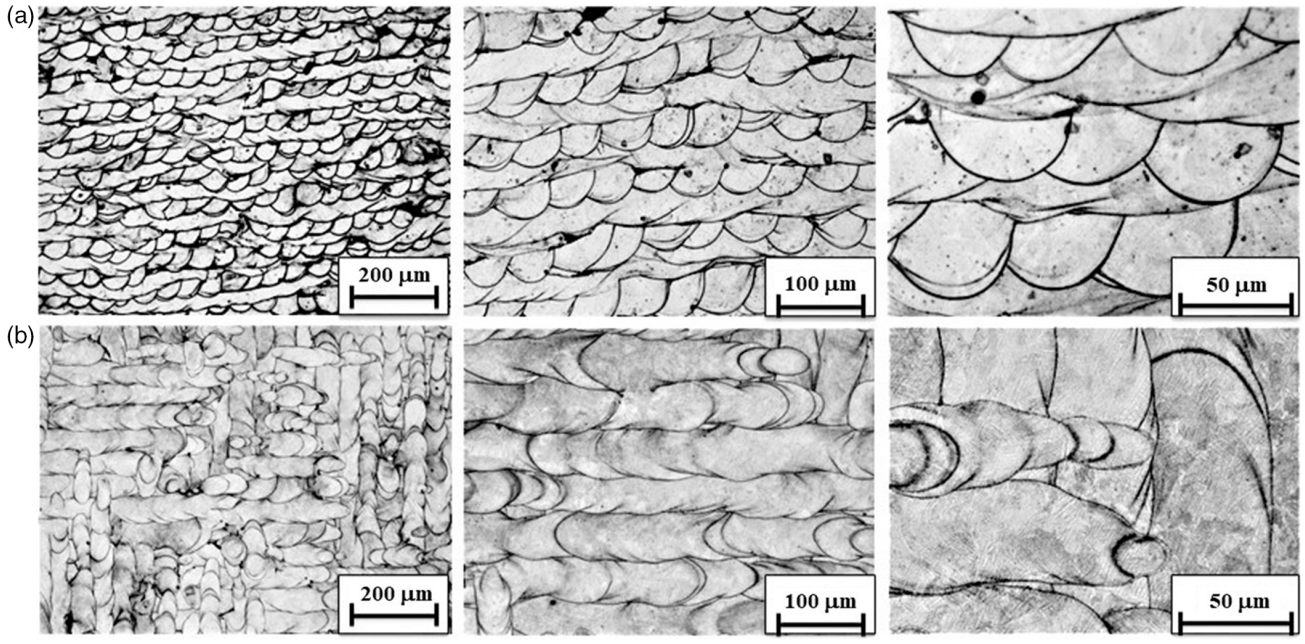

Figure 4. Optical micrographs of the a) CoCrMo longitudinal and b) transversal sections of AB conditions.

for a short time.[18] In addition, as the transformation is conditioned on the grain size, for fine SLM structures, this change is repressed, resulting in the predominant γ phase.[48]

In agreement with literature,[18,46,47] the AB microstructure of this study consisted of a fine cellular structure, where the γ phase is predominant (Figure 4 and 7A,B**)** and small precipitates that seemed concentrated especially on the grain boundary (GB) between the grains formed by solidification of the liquid front. In fact, in contrast to the microstructure obtained from traditional processes, in this case, there is no evidence of needle-like structures.[18,21] In particular, Kajima et al.[21] affirmed that ε phase is present only after an additional HT and the volume fraction between γ and ε varies upon the HT temperature, but γ remains as the predominant phase (≥75% volume fraction). It is important to point out that recent literature[19] affirms that martensite is present (maximum 30%) in the AB condition, after several postheating cycles caused by additive formation. Therefore, according to the literature, there is the dominance of Co-based γ matrix phase in the AB condition in many works, but the microstructure of SLM can be heavily dependent on operational parameters, such as line and island scan strategy [18,49] and polished/unpolished surface.[50] In addition, the rapid sequence of continuous cooling/heating in the SLM process (constitutional supercooling criterion) allows obtaining cellular growth,[51] with the formation of small, homogeneous, and uniform grains.

The observed AB microstructure leads to a reduction in dislocation mobility and accordingly high hardness and mechanical strength could be obtained. In this case study, the volume fraction of ε phase calculated with image analysis is ≈10%.

The micrographs of the different HTs and HIPs are shown in Figure 5–7. It is worth clarifying that the HTs differ significantly. The samples treated at 800 °C underwent stress relieving, whereas at 1150 °C annealing with recrystallization occurred. The changes of microstructural phases and the volume fractions of γ and ε phases clearly depend on temperatures and cooling methods of the HTs. Macroscopically, the micrographs collected from the longitudinal section of the specimens heat treated at 800 °C for both times (20 min and 2 h) still show a characteristic weld-like structure. Also, from a transversal view, no substantial changes occurred with respect to the AB condition, displaying an elongated structure according to the laser path. At higher magnifications (Figure 7), the most significant differences are represented by the presence of γ + ε phase; in particular, ε phase is observed into the cellular structures with a major amount of intermetallic precipitations and/or carbides. Through image analysis it is estimated that for samples heat treated at 800 °C the ε amount increases to 18% and 20% for 20 min and 2 h, respectively.

The HT at 800 °C promotes the formation of ε-Co, which should lead to an increase in resistance and Young's modulus, as confirmed by Turrubiates−Estrada et al.[52] Also, the isothermal time temperature transformation (TTT) diagram of CoCr27Mo5C0.23, adapted from Prior and coworkers,[53] indicated that heat treating at 800 °C encourages the formation of ε-Co and intermetallic precipitations and/or carbides.

Increasing the aging time from 20 min to 2 h at 800 °C aging temperature, the solidification structure is less defined and, according to Hitzler et al.,[18] this phenomenon can be ascribable to partial recrystallization. In addition, Kajima et al.[21] proved that HT at 800 °C for 6 h can promote an increment of volume fraction of ε-Co of around 20–25% in SLM samples. The formation of the second phases in a sufficiently fine distribution (high undercooling) could be the origin of an increase in the mechanical properties. The increased precipitation could be attributable to a decrease in solid solubility of carbide elements in Co matrix.

HTs at 1150 °C made the microstructure more homogenized in comparison with AB samples. A completely modified microstructure could be immediately seen, as shown in Figure 5–7. The HT at 1150 °C led to a complete modification of the

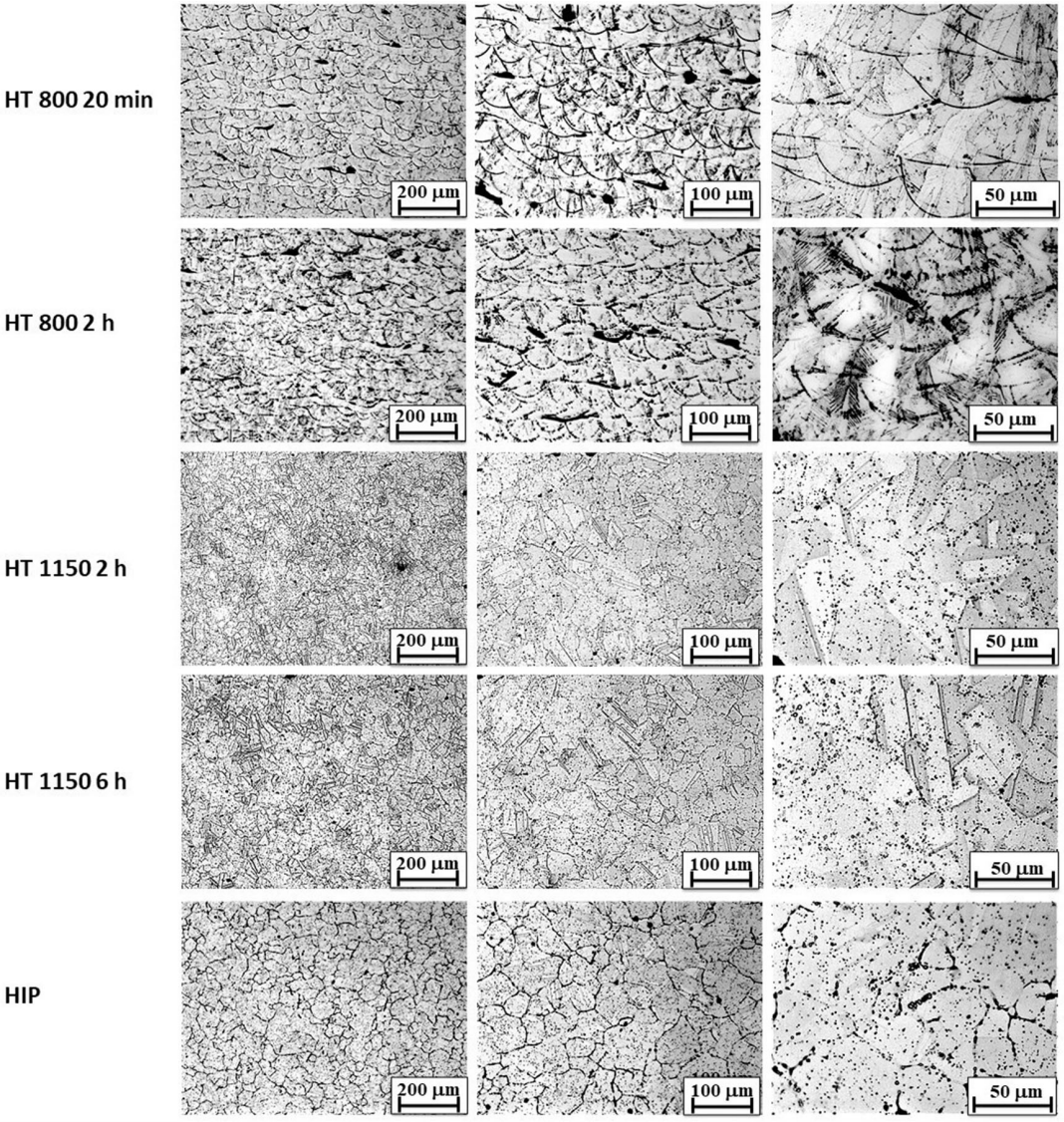

Figure 5. Optical micrographs of the SLM CoCrMo longitudinal sections of heat-treated and HIPed conditions.

microstructure, whereby the stacking scheme of single-weld beads was no more visible. The carbides were highly dissolved, resulting in very small precipitates within the grains and on the GBs. Longitudinal and transversal micrographs (Figure 5 and 6) showed the presence of equiassic grains without differences of orientation and size, confirming that the complete recrystallization occurred. As a consequence, the microstructure revealed isotropy and uniform mechanical behavior was expected. The micrographs collected on samples heat treated at 1150 °C for 2 h showed the presence of γ+ε phases. The grains were more evident and a typical face-centered cubic (FCC) γ grain structure with some twins was visible; on the contrary, the volume fraction of the ε phase decreased with respect to HTs at 800 °C. The presence of ε phase decreased with increasing HT temperature, approaching zero at 1150 °C. The increase in holding time revealed no substantial changes in the microstructure but it seemed that more diffusion could occur and carbides could dissolve in the matrix causing a decrement of the precipitates' concentration in CoCrMo alloy with increasing solution time.

The micrographs showed the presence of large number of annealing twin boundaries, characteristic of a low-stacking fault energy material, indicating that recrystallization occurred. These results are in agreement with the literature[18–21] that indicated for SLM CoCrMo alloy heat treated at 1150 °C the prevalence of γ phase with very low values of ε phase (lower than 5%).

The HIP-treated samples evolved in well-defined coarse grain structures that is proof of a complete recrystallization; all precipitates dissolved into the matrix, increasing the elongation of the specimens and decreasing their hardness and tensile yield strength.[54] Even in this case, both in the longitudinal and in the transversal view (Figure 5 and 6), the isotropy was verified by the presence of the equiaxed grains and the complete

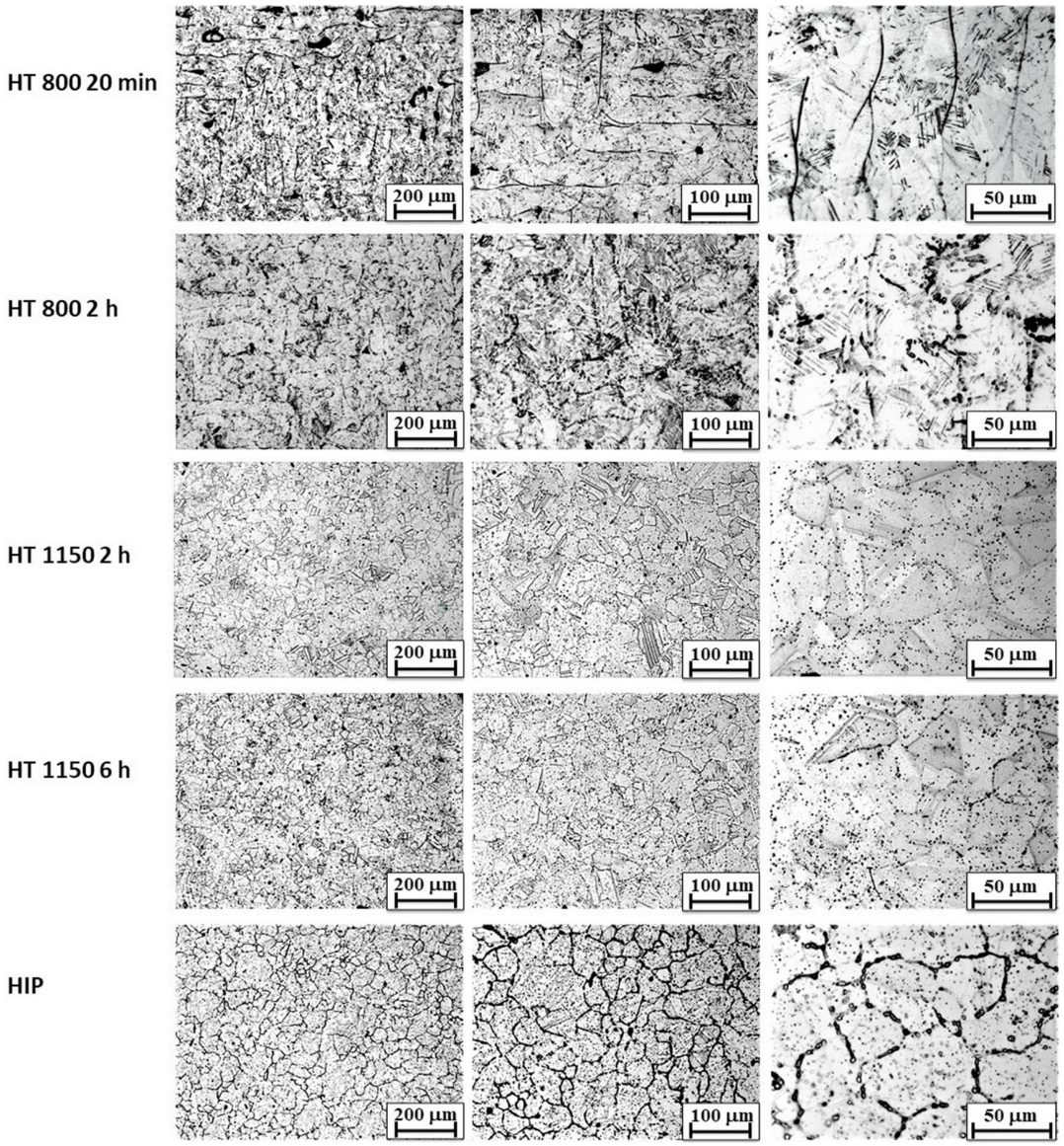

Figure 6. Optical micrographs of the SLM CoCrMo transversal sections of heat-treated and HIPed conditions.

recrystallization. In particular, the microstructure of the HIP was homogenous with a prevalent presence of γ phase, as confirmed in the study by Haan et al.[55] This result may be due to the slow cooling rate typical of the HIP process, which favored its formation. The image analysis confirms the minimal presence of ε phase, which is approximately between 3% and 5% both for the samples heat treated at 1150 °C and for the HIPed ones.

The high temperatures of HT at 1150 °C and HIP treatments promote the formation of annealing twin boundaries in CoCrMo alloys during recrystallization from the stacking fault bands.[56–58] In particular, in the HT at 1150 °C specimens, many annealing twin boundaries were detected into equiaxed grains, whereas, for HIP, a decrease in annealing twins was noted with respect to HT ones. The presence of a large fraction of annealing twins contributed to the increase in ductility of the material, and the plastic strain was significantly reduced, thanks to HT that suggested a stress relief process.[59]

HIP is an effective thermomechanical process that can influence the grain structure: it diminishes the porosity and it should reduce the thermal stresses. Therefore, microstructural evolution during the HIP process is fundamental and dependent on powder parameters, optimized cycle, and eventual post-HIP HT, that have a critical role in the development of the final microstructure.

It is important to highlight that HT had a cooling step in argon with a cooling rate of about 5 °C s^{-1}, whereas the cooling step of the HIP process was in the furnace with argon protection with an estimated cooling rate of about 0.09 °C s^{-1}. The HT faster cooling generated a finer microstructure, more advisable for structural purposes, whereas for the HIP, grain growth occurred and larger grains could be observed also in comparison with AB specimens.

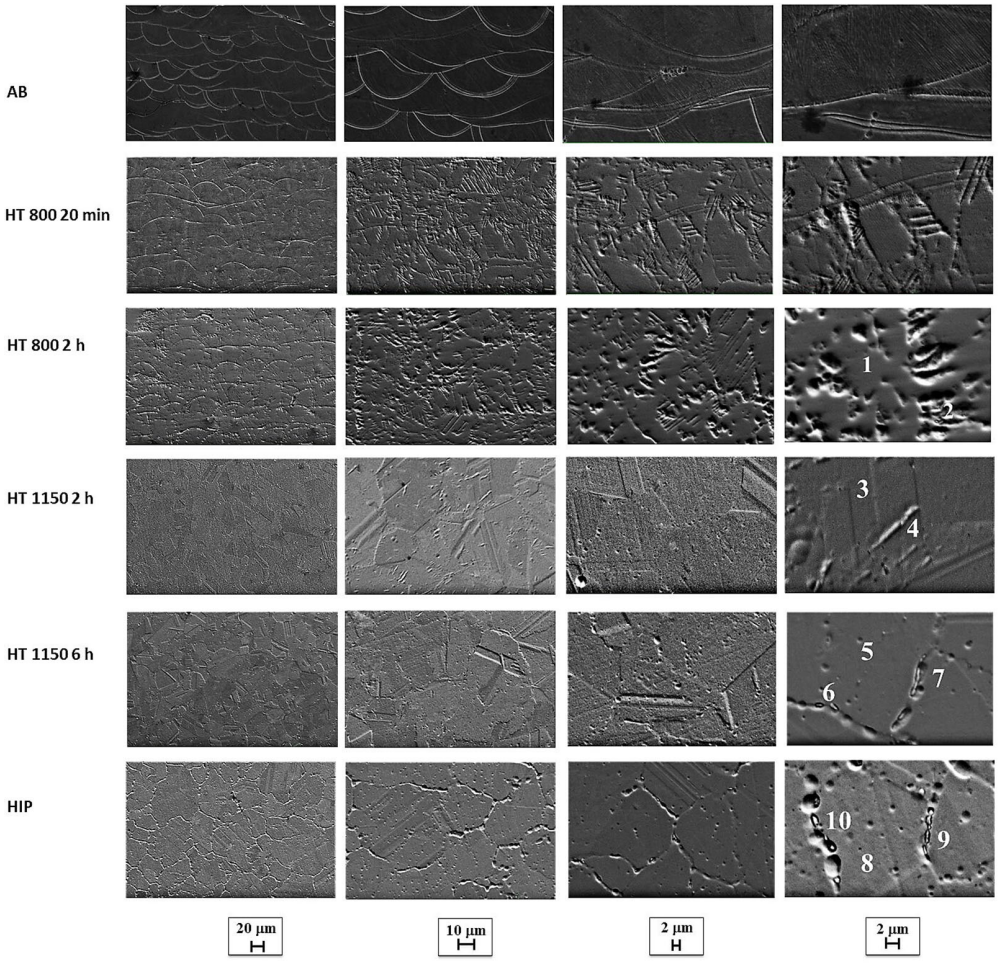

Analysis	Si	Cr	Co	Mo
1	1.5	30.7	63.2	4.6
2	0.7	35.3	54.5	9.5
3	1.1	30.3	62.9	5.7
4	0.8	35.2	52.8	11.2
5	0.8	31.0	62.7	5.5
6	1.0	35.6	52.8	10.6
7	0.6	33.8	54.7	10.9
8	0	31.4	63.0	5.6
9	0.9	36.4	53.4	9.3
10	1.2	34.2	54.1	10.5

Figure 7. SEM/SE micrographs of the SLM CoCrMo longitudinal sections at the AB state and after HTs and HIP conditions, and some examples of their Co, Cr, and Mo contents in wt% determined by EDS.

Punctual analyses conducted with SEM/EDS (some examples shown in Figure 7) indicated that the specimens heated to 800 °C contained very fine precipitates both inside the grains and at the GBs. After heating at 1150 °C and after HIP, needle-like precipitates grew along the GBs. The Cr and Mo contents were higher in the precipitates than in the alloy matrix and were more evident

in HIP condition. It can be inferred that these Cr- and Mo-rich precipitates in the FCC Co base phase existed mainly as $M_{23}C_6$ carbides.[60]

3.2. Hardness and Tensile Test

A summary of the results of mechanical characterization (tensile test and hardness) is shown in the graphs of **Figure 8**. At this point, it is important to highlight that γ phase is softer than ε phase so that the relation between tensile properties, hardness, and microstructure with the different treating conditions studied in this work can be properly understood. In fact, as a consequence of the changes in microstructure after HIP or HTs, a deep modification of mechanical behavior was observed with respect to the AB case.

For all cases, considering the values of yield stress $R_{p0.2}$ and ultimate tensile strength R_m, these properties satisfy the minimum requirements stated in class 5 of ISO 22674 standard,[61] concerning metallic materials for parts requiring high stiffness and strength, such as fixed and removable restorations and appliances in dentistry. The influence of the HT condition was quite marked. When the material was heat treated at higher temperatures (i.e., 1150 °C) or HIPed, yield stress $R_{p0.2}$ slightly decreased, whereas ultimate tensile strength R_m was almost unchanged after post-treatments. A remarkable increase in Young's modulus E and elongation at break A [%] could be appreciated. In particular, the evolution was more evident when considering the improvement of ductility related to the noticeable increase in elongation at failure (At), from ≈6% to 25−30%, as a consequence of recrystallization processes. The AB, 1150 °C (2 and 6 h), and HIP specimens consisted almost entirely of the γ phase; therefore, the reasons for these differences in mechanical properties can be associated with the differences in the grain size and the precipitate distribution. In the AB condition, the fine cellular structure and small precipitates reduced the dislocation mobility, leading to high R_m, $R_{p0.2}$, and hardness. After 1150 °C HT and HIP, the completed recrystallization, grain coarsening, and precipitates' solubilization resulted instead in a reduction of the same properties.

When considering HT at lower temperatures (800 °C), a different effect could be observed. While the increase in ultimate tensile strength R_m was limited, a marked increase in the yield strength $R_{p0.2}$, increasing with HT duration, was instead evident and associated with a significant increase of elastic modulus E and a very limited change in elongation at break A [%].

These results were interpreted as a consequence of a combination of different factors, such as the transformation phase ε → γ which occurred, according to microstructural observations, for the HT at 1150 °C samples and not for the HT at 800 °C samples (in the latter γ and ε coexist and the HCP lattice is more difficult to deform) and the role of carbides, which are the principal sources

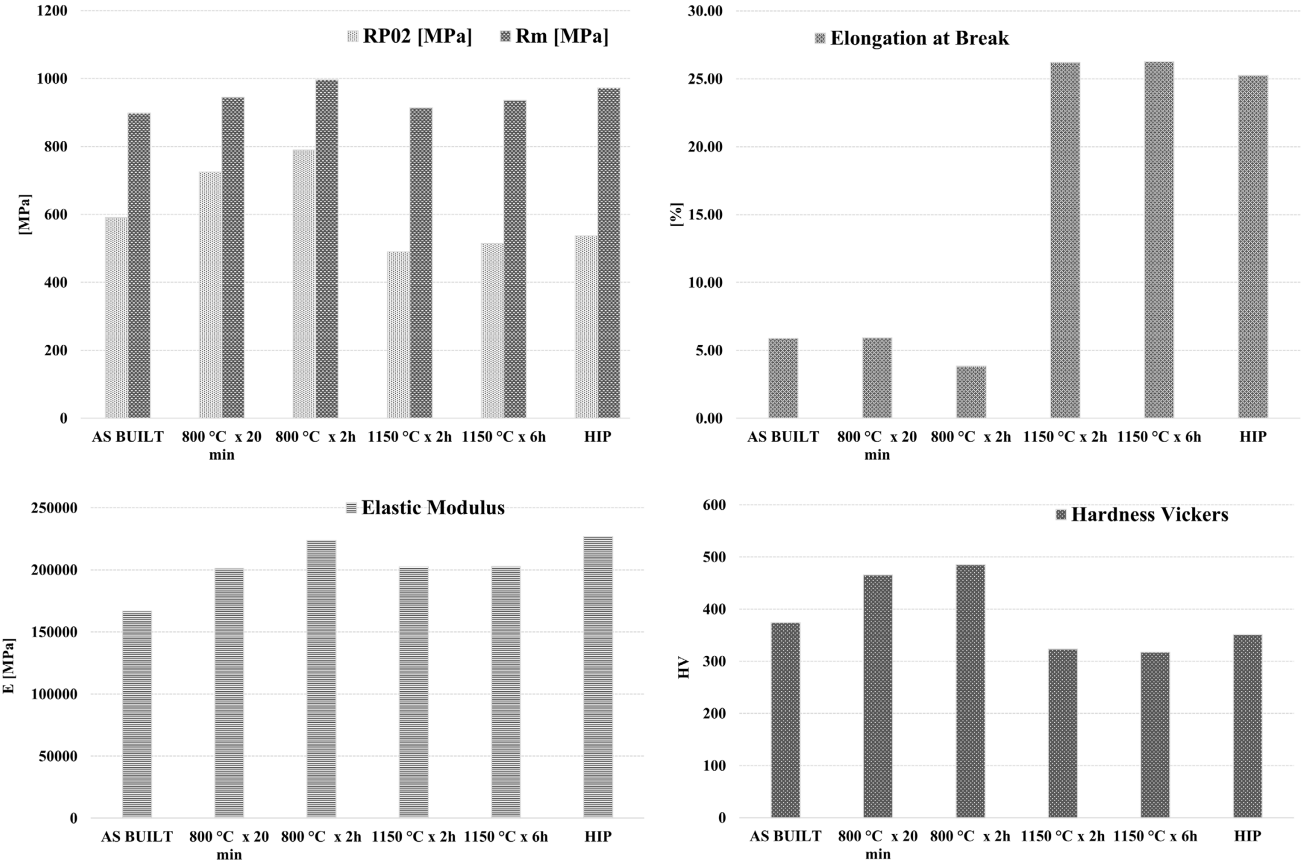

Figure 8. Mechanical properties (R_{p02}, R_m, elongation at break, and elastic modulus, respectively) and hardness vickers (HV) values for SLM CoCrMo alloy at AB state and after HTs and HIP conditions.

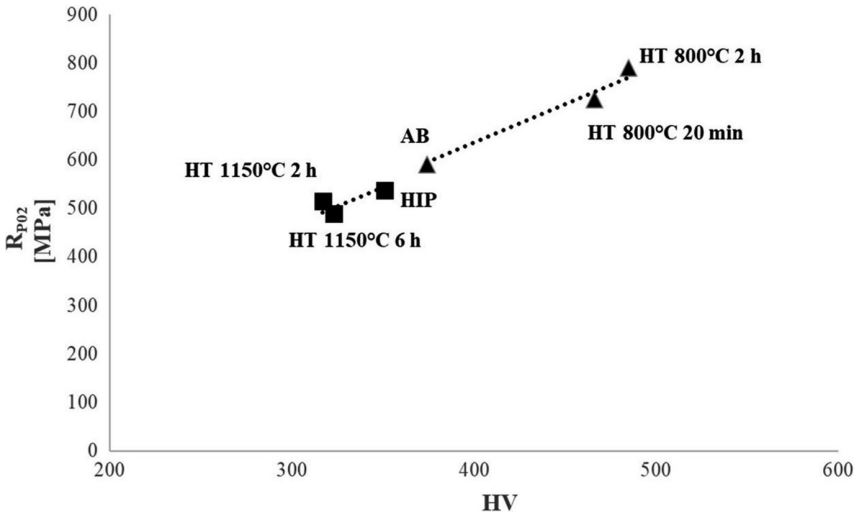

Figure 9. The trend of hardness HV with respect to R_{p02}.

of strengthening of the material (permanence for 2, 4, or 6 h of treatments at 1150 or 1200 °C dissolved part of them).

Furthermore, the effect of the different holding times was investigated, to understand the best compromise between HT conditions, mechanical properties, and treatment costs. Considering the HTs carried out at 800 °C, an increase in the properties such as R_m, E, and $R_{p0.2}$ (with decrease in A%) was observed when going up from 20 min to 2 h, suggesting that a longer steady temperature time could be useful and necessary to increase the tensile resistance.

With regard to the HT carried out at 1150 °C, the HT time increased and led to a slight increase in R_m, whereas E and A% remained unchanged and $R_{p0.2}$ decreased, indicating that long-term maintenance in the furnace is not necessary and is actually detrimental for some properties.

Hardness tests were conducted to have a complete description of the static behavior of the SLM CoCrMo alloy. Considering HV hardness values of AB samples, slightly lower values were found when compared with literature.[41] These were further decreased by HT at higher temperatures and with HIP, whereas the opposite effect was observed for HT at 800 °C, increasing with HT duration.

In particular, it emerged that the HTs carried out at 1150 °C and the HIP treatment contributed to the lowering of the hardness indexes of about 17–23% compared with the AB sample, whereas the heat-treated samples at 800 °C showed an increase in hardness of about 10−15% compared with the AB hardness. The hardness data are in agreement with microstructure analysis and tensile test results. In fact, as shown in **Figure 9**, the increase in HV appears to be well correlated with a progressive increase in yield stress $R_{p0.2}$, especially for HT at 800 °C.

The marked influence of HT on the stress strain behavior of SLM CoCrMo for different conditions investigated in the present work is clearly shown in **Figure 10**.

In Figure 10, dotted lines refer to experimental data and continuous lines to a fitting with a Ramberg−Osgood model, as per Equation (1).

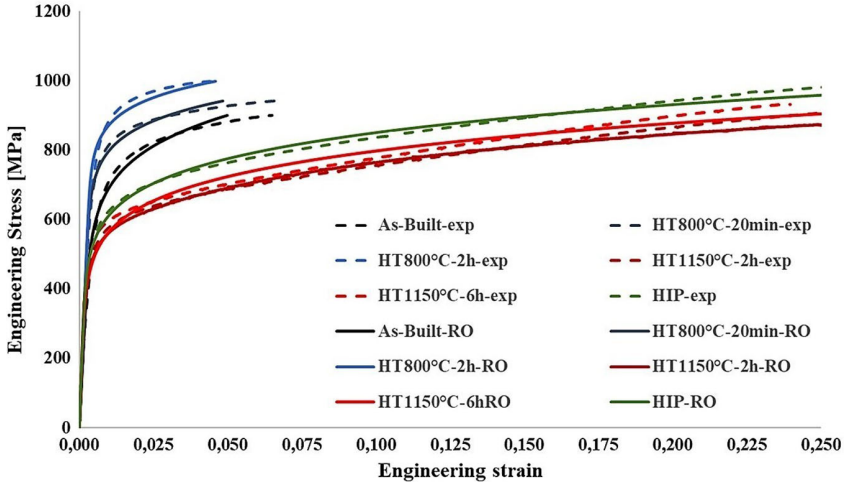

Figure 10. Stress−strain curves.

Table 4. Estimation of Ramberg–Osgood constants (n and H) for each studied condition.

Sample condition	n	H [MPa]
AB	0.130	13 49
HT 800 °C 20 min	0.084	1224
HT 800 °C 2 h	0.0691	1244
HT 1150 °C 2 h	0.138	1023
HT 1150 °C 6 h	0.134	1091
HIP	0.127	1145

$$\varepsilon = \frac{\sigma}{E} + \left(\frac{\sigma}{H}\right)^{\frac{1}{n}} \quad (2)$$

in which n is a strain-hardening exponent and H is an additional constant. For each set of stress–strain data and following the study by Lewinsohn,[62] the Ramberg–Osgood parameters were obtained by making a log–log plot of stress versus plastic strain, assuming for yield stress the R_{p02} values previously reported. Values of n and H are shown in **Table 4**.

The fracture surfaces of the tensile specimens observed in all studied conditions are shown in **Figure 11**. The AB and the 800 °C (20 min and 2 h) surfaces reveal an overall flat fracture attributable to a "quasi-cleavage" fracture mode. In particular, the nucleation zone was located at discontinuity sites such as unmelted powder particles, resulting from the lack of fusion of the powder during the SLM process. The presence of unmelted powder may also explain the reduced tensile ductility. The presence of some wedge-type cracks that were also found in previous studies can be noted [1,49,63] and this may be initiated through the cleavage fracture on the {1 1 1} plane, where stacking faults are developed.

Under HT at 1150 °C (2 and 6 h) and HIP conditions, the fracture surfaces are characterized by typical transgranular fractures with the total presence of microdimples, indicating that these were extremely ductile fractures. Moreover, these fracture surfaces show the presence of defects, and some micrometer-size unmelted particles also appeared in the HIP sample.

3.3. Wear Measurements

The influence of HT on tribological behavior was analyzed considering the wear track, the COF, and the specific WR (load of 5 N, sliding distance 50 m, dry reciprocating sliding conditions). As shown in **Figure 12** and **13**, the structures of the worn surfaces of the samples and the wear debris were analyzed using SEM, equipped with EDS, to understand the prominent wear mechanisms taking place during the test. The values of stabilized COF and specific WR for the different conditions are instead shown in **Figure 14** and **15**, respectively.

The wear scar geometry was also studied to obtain information on the wear mechanism and some differences could be clearly observed for the dimension and morphology of the tracks when considering the worn surfaces shown in Figure 12. In particular, AB sample shows an almost smooth wear track, with shallow grooves and only a few debris on the worn surface; the dimension of the wear track is about of 342 μm. HIPed sample had a wear morphology very similar to AB, but the extension of the damaged surface seemed lower and the track width was reduced to about 314 μm. The HTs at 800 °C exhibited a very similar wear track with respect to AB sample, but for these conditions, the surface was smoother and the track width was slightly smaller, measuring about 330 and 334 μm (for 20 min and 2 h, respectively).

When considering the wear tracks of the samples treated at 1150 °C, it is instead possible to note the presence of a different friction behavior. In this case, it can be clearly seen that plastic deformation, tearing trace and plough along the sliding direction, occurred on the surface of the alloy. The dimension of the worn track is 355 μm for the treatment at 2 h and about 370 μm for that at 6 h. For this last condition, the higher width of the worn surface could be related to the predominance of abrasive wear and plastic deformation. From the earlier analysis, it can be inferred that the main wear mechanisms of SLM CoCrMo alloy, under the test conditions used, are adhesion wear and abrasive wear, with different effects depending on temperature and time of the HT condition examined. In general, for the same treatment temperature, as the holding time increases, the

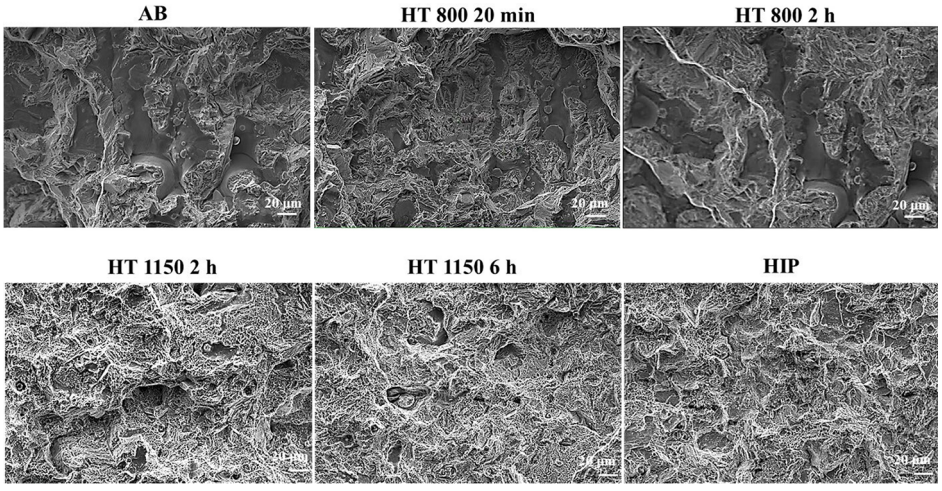

Figure 11. Fracture surface morphologies of specimens after tensile test in AB state and after HTs and HIP conditions.

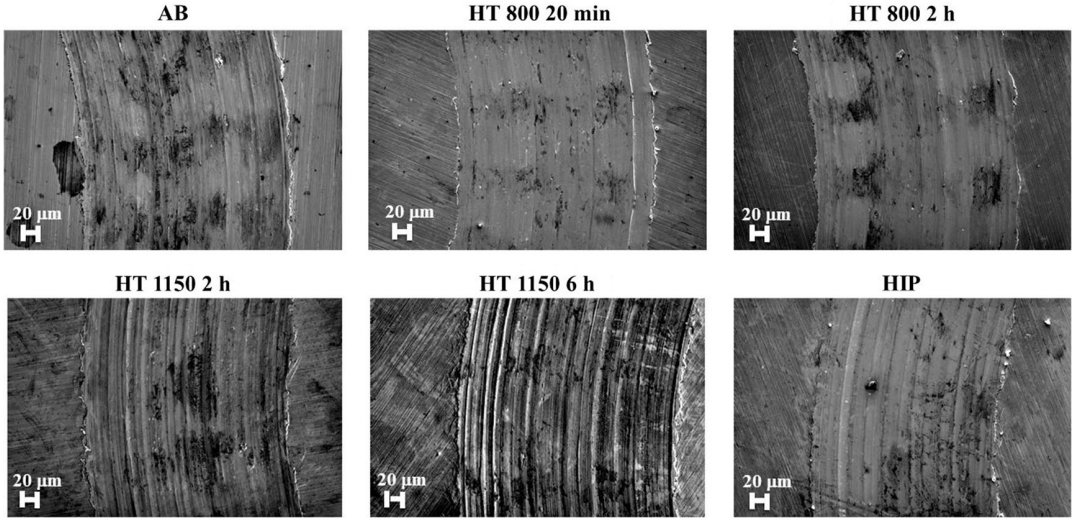

Figure 12. SEM morphology of worn surfaces of the samples after the pin-on-disc test with load of 5 N, sliding distance 50 m, and dry reciprocating sliding conditions.

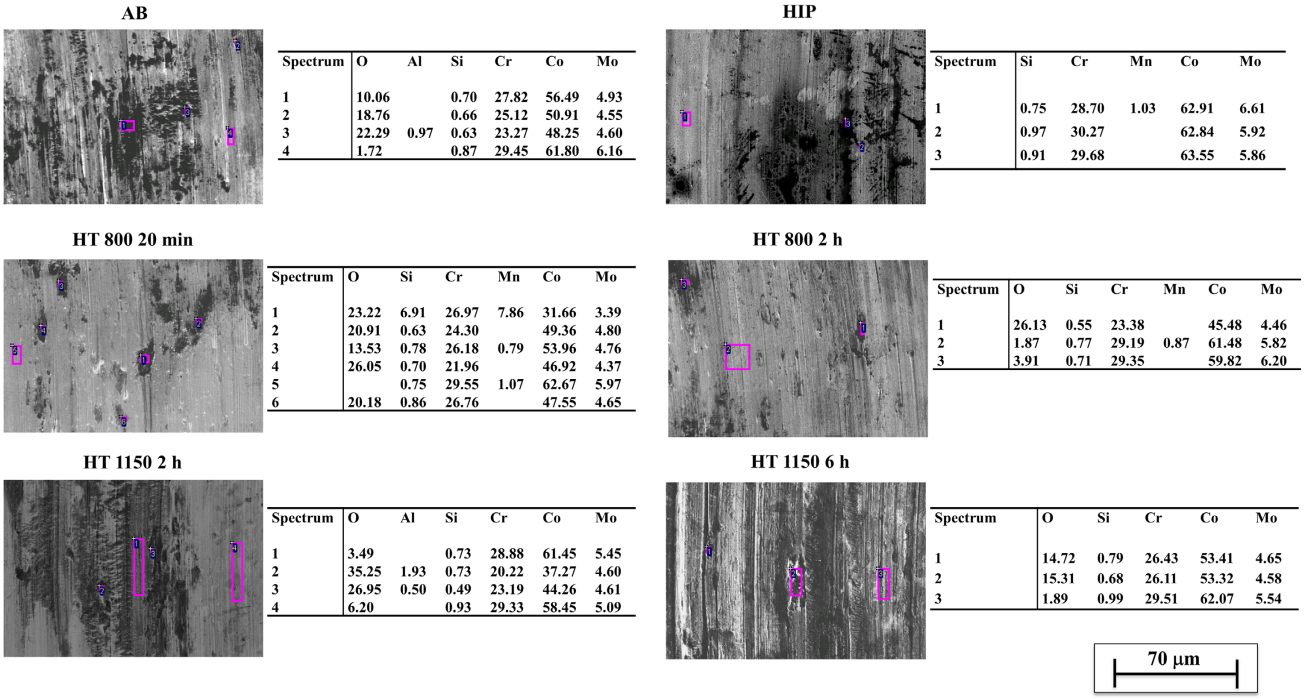

Spectrum	O	Al	Si	Cr	Co	Mo
1	10.06		0.70	27.82	56.49	4.93
2	18.76		0.66	25.12	50.91	4.55
3	22.29	0.97	0.63	23.27	48.25	4.60
4	1.72		0.87	29.45	61.80	6.16

Spectrum	Si	Cr	Mn	Co	Mo
1	0.75	28.70	1.03	62.91	6.61
2	0.97	30.27		62.84	5.92
3	0.91	29.68		63.55	5.86

Spectrum	O	Si	Cr	Mn	Co	Mo
1	23.22	6.91	26.97	7.86	31.66	3.39
2	20.91	0.63	24.30		49.36	4.80
3	13.53	0.78	26.18	0.79	53.96	4.76
4	26.05	0.70	21.96		46.92	4.37
5		0.75	29.55	1.07	62.67	5.97
6	20.18	0.86	26.76		47.55	4.65

Spectrum	O	Si	Cr	Mn	Co	Mo
1	26.13	0.55	23.38		45.48	4.46
2	1.87	0.77	29.19	0.87	61.48	5.82
3	3.91	0.71	29.35		59.82	6.20

Spectrum	O	Al	Si	Cr	Co	Mo
1	3.49		0.73	28.88	61.45	5.45
2	35.25	1.93	0.73	20.22	37.27	4.60
3	26.95	0.50	0.49	23.19	44.26	4.61
4	6.20		0.93	29.33	58.45	5.09

Spectrum	O	Si	Cr	Co	Mo
1	14.72	0.79	26.43	53.41	4.65
2	15.31	0.68	26.11	53.32	4.58
3	1.89	0.99	29.51	62.07	5.54

Figure 13. SEM micrographs and EDS analysis of the wear track of the samples after the pin-on-disc test with load of 5 N, sliding distance 50 m, and dry reciprocating sliding conditions.

damage to the worn track seems more noticeable, as shown in Figure 12 and 13. In particular, for the case of 1150 °C, it is evident from Figure 13 that in some regions the oxide layer spalled away due to third body abrasion, resulting in craters' formation, indicating the prevalence of abrasive wear.

EDS analysis highlighted the presence of oxygen in all samples except for HIP. Unfortunately, while this suggests the presence of an oxidative wear mechanism, this analysis does not provide any information about the nature of such oxides, which can actually lead to significantly different interpretations of the mechanisms involved. As a matter of fact, these oxides could either play a negative or positive role, depending on the oxide type. If the sample is covered by a nonprotective oxide layer that is constantly removed, a fresh surface is always in contact with new asperities, leading to higher damage. On the contrary, if the oxide is not detached, the formation of a protective layer prevents further damage to the sample surface with a decrease in the wear depth and the COF.[64]

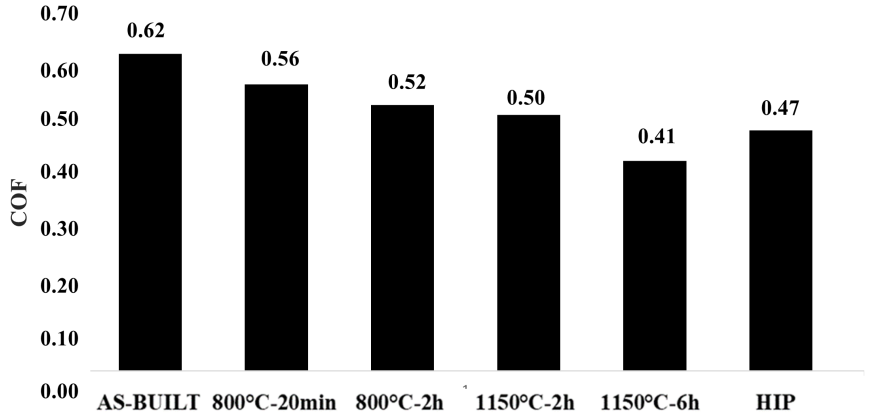

Figure 14. Reciprocating sliding test 5N-50m: COF.

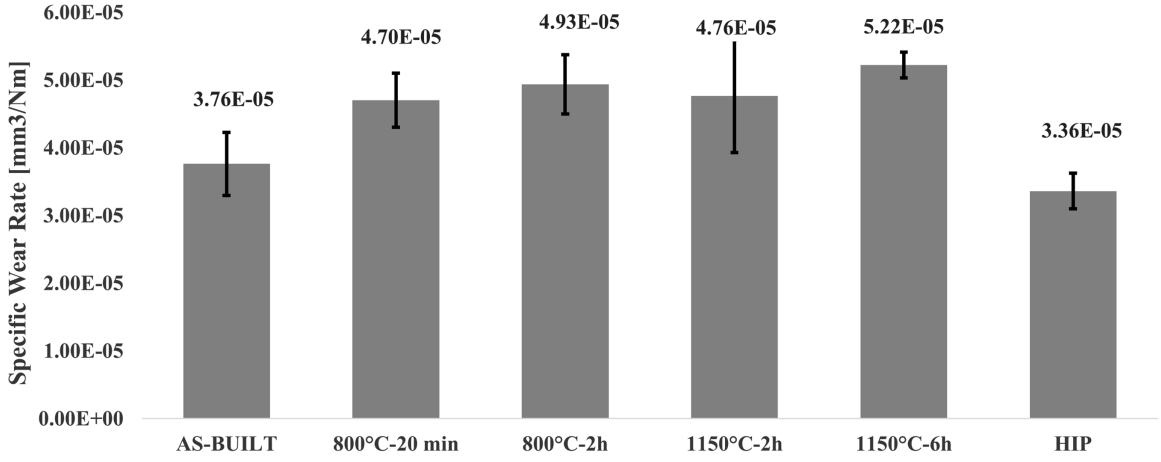

Figure 15. Reciprocating sliding test 5N-50m: specific WR.

Regarding the values of COF (Figure 14) within the sliding distance examined, AB showed a COF value of about 0.62. This result is comparable with the COF of 0.55 ± 0.05 reported in the study by Duran et al.[28] for SLM CoCrMo alloy under dry conditions in the AB state. Interestingly, it should be remarked that in the study by Duran et al.[28] the COF of the alloy produced with SLM technique was also compared with that of the traditional cast alloy. It was found that the COF of the cast alloy was higher (0.73 ± 0.05), demonstrating better wear resistance of the SLM sample. Although the value obtained in this work for the AB sample is slightly higher than that obtained in the work of Duran et al,[28] the comparison with reference cast alloy confirmed the same trend. The COFs of all treated samples were lower than the AB condition, indicating that the treatments improved the friction behavior. However, COF values of different treatments are quite similar, with the partial exception of the treatment at 1150 °C for 6 h that exhibited the lowest COF value and, at the same treatment temperature, the COF tends to decrease as the holding time increases.

In Figure 15, the results of the specific WR for the different conditions are summarized; the specific WR was calculated as the rate at which material is removed per unit load and the results were obtained after analysis of track width and depth. The range of specific WR values found in this study goes from 3.36 to 5.22×10^{-5} mm^3 (Nm)$^{-1}$. As a reference, under similar conditions, values of 6.94×10^{-5} and 0.81×10^{-5} mm^3 (Nm)$^{-1}$ were reported for cast and SLM CoCr alloys respectively in the study by Duran et al.[28] In general, the AB condition exhibited lower WR when compared with HT samples, with the notable exception of HIP, that showed the lowest WR among all conditions. Moreover, while the treatments at 800 and 1150 °C for 2 h showed similar specific ware rates, it is worth noting that the sample treated at 1150 °C for 6 h showed a low COF coupled with a high specific WR.

In **Figure 16**, specific WRs are reported as a function of hardness HV, as measured on the initial surface (a) and on the worn surface of the track after the test (b). Interestingly, some different trends could be noticed if considering samples treated at 1150 °C or with HIP as one group and samples treated at 800 °C and AB as another group. For samples treated at 1150 °C or HIPed, the WR decreased significantly with initial HV, whereas the opposite trend was observed when considering HV measured on the worn surface. Instead, for AB and samples treated at 800 °C, specific WR increased, considering both initial HV and worn surface. This behavior can be related to the fact that the samples with initially higher HV (i.e., those treated at 800 °C) exhibited low

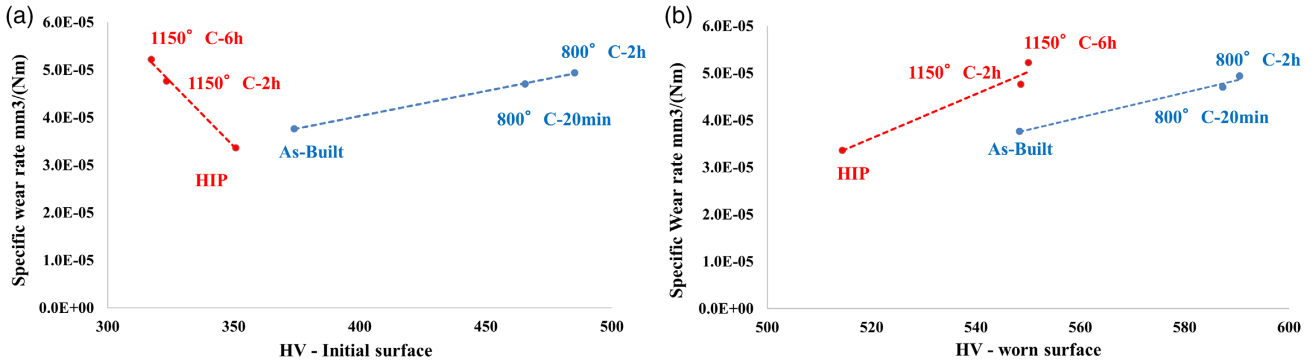

Figure 16. Specific WR as a function of a) initial hardness and b) worn track hardness.

variation of their hardness on the track after the wear tests, whereas the HV change after sliding was marked on the samples with initially lower hardness (i.e., those treated at 1150 °C), indicating that load-induced plastic deformation occurred on the track, modifying material behavior.

When comparing the two groups, contrasting trends can also be evidenced: samples with different HVs on the worn surface exhibiting similar specific WRs (i.e., AB vs. HIP or HT at 1150 °C vs. HT at 800 °C) and samples with similar HVs on the worn surface (i.e., AB vs. HT at 1150 °C) exhibiting different WRs. This suggests that hardness is likely not the only factor involved, and different wear mechanisms are acting. Notably, the lowest value of specific WR was obtained for HIPed samples, featuring the lowest levels of HV on the worn track and porosity. It is also noteworthy that in AB and HIPed samples, the γ phase should be predominant, in contrast with heat-treated samples at 800 °C, where the presence of $\gamma + \varepsilon$ phases was noticed. In addition, metal carbides could play a fundamental role and their influence has been the focus of study in previous tribochemical researches on cast or SLM CoCr alloys. In general, the presence of fine carbides helps strengthening the alloys and a better wear resistance is naturally expected. Nevertheless, even very hard carbides could be torn off in the wear process leading to third-body wear. Dislodged carbide particles could subsequently lead to abrasive wear and low wear resistance, as suggested by surface scratches and grooves observed parallel to the sliding directions in some studies on the wear behavior of CoCr alloys.[65,66] As a result, their exact effect is yet to be clearly identified,[67] as confirmed by different findings reported in literature. For example, in a comparative study on electron beam melting (EBM) titanium and CoCr alloys,[68] higher wear resistance of CoCr samples was attributed to the presence of protruding carbides, with irregular shape and size, which isolated the matrix from the asperities of the counterball, resulting in less material being removed. In contrast, in the study by Tan et al.,[69] the presence of a weak incoherent interface between the GB carbide and one side of the γ-Co grains was observed, which could more likely lead to carbide dislodgment with detrimental effects on tribocorrosion behavior.

Considering the present study, as previously discussed, very fine and small precipitated were observed both inside the grains and at the GBs for heat-treated specimens. These samples, compared with AB, showed higher WRs possibly confirming a negative effect, although even in the HIP condition, Cr- and Mo-rich precipitates in the FCC Co base phase existed.

As a concluding remark, the interpretation of results is not straightforward, because of the combination of several factors such as hardness, microstructure, porosity, presence of carbides, nature of debris, and formation of oxides on, which depends on the type of wear mechanism.

Overall, HIP seems to be the best treatment in terms of tribological behavior under present testing conditions. In fact, it has a low COF, a smooth and relatively small trace of wear without tears, and no traces of oxide on the worn surface, associated with the lowest specific WR. In this case, the prevailing wear mechanism seems to be adhesive wear. The HTs at 800 °C and 1150 °C for 2 h have a similar COF and WR, although after observing the worn surface, both HTs at 800 °C could be deemed to be more suitable to withstand wear, due to the presence of mainly adhesive wear, which creates more favorable tribological conditions. In addition, the morphology of worn surfaces presented smooth nondelaminated regions, which could be associated with oxidative wear. This may contribute to protecting the sample surfaces, because in the presence of a hard oxide layer, the WR gradually decreases, especially the adhesive wear. Previous studies have also shown that dominant adhesive wear may result in increased COF.[70,71] In particular, Trevisiol et al.[70] analyzed the effects of martensite volume fraction, hardness, normal load, and abrasive particle size on COF, WR, and wear mechanisms. The article highlighted that low normal load minimizes the WR, whereas high normal loads minimize the COF. For low martensite volume fractions, adhesion wear mechanisms are predominant. In contrast, for high martensite volume fractions, the cutting wear mechanism is predominant. Similarly, fine abrasive particles yield to predominant adhesion whereas coarse abrasive particles yield to predominant plowing with severe plastic deformation. The smallest abrasive particles minimize the WR, whereas intermediate-sized particles minimize the COF. The WR and the COF decrease with increasing martensite volume fraction. In contrast to the WR, the COF becomes insensitive to the martensite volume fraction for high normal loads. It is also noticed that there are combined effects of martensite volume fraction and abrasive particle size on wear mechanisms.

Finally, among the different conditions examined, the samples treated at 1150 °C for 6 h exhibited a peculiar combination of lower COF and higher WR, which is difficult to interpret,

although some hypotheses could be formulated to explain this particular behavior. The lower COF value may depend on the different effects that the load has on the material as a function of the microstructure generated by the HT. For this specific condition, 5 N could be a relatively high normal load, and a sort of equilibrium state with mating surface can be reached more quickly. Consequently, COF attained a low value in the steady state due the localized decrease in asperity damage, which would have caused instead high perturbation if a lower normal load was used.[72,73]

In addition, it was observed that this sample had the most debris, so it could also be hypothesized that during the test the debris of oxides remained in the wear track and were better compacted on the contact surface. This compact oxide film then acted as a protective layer on the metal surface, also concurring to the lowering of the COF for this sample.[73–77]

In contrast, the higher specific WR value, which is in agreement with the plastic deformation, depth, and morphology of the worn track analyzed, could be a consequence of the prevalence of abrasive wear or of the presence of some local subsurface porosity not initially detectable.

As a final remark, in the present work, we mainly considered the effect of HTs and HIP but of course, when considering methods to enhance the wear resistance of additively manufactured metal alloys, other approaches are possible. As already mentioned in the Introduction of this work, a first alternative is provided by surface treatments, as discussed, for example, for a DMLS 17-PH4 steel in the study by AlMangour et al.,[23] where an improvement in wear resistance after shot peening was attributed to the formation of a strong fine surface layer (i.e., grain refinement) and work-hardening effect. As tribological properties are strictly related to microstructure, another option is to investigate the possibility to improve tribological properties by tuning the laser processing parameters, thus avoiding the need of post-treatment.[24,25] For AM CoCr alloys, these approaches were not reported yet and might represent an interesting field for future research.

4. Conclusion

In this study, effects of different HTs on mechanical properties, wear, and microstructural features of Co28Cr6Mo fabricated via SLM were investigated. The evidences presented in this research can be summarized as follows. 1) Regarding porosities, it was found that size and quantity fall within an acceptable range for SLM products and the regular shape was predominant. The strongest reduction of regular-shaped defects was found for HIP treatment due to porosity flattening and shrinkage effects. In HT at 1150 °C, a softer reduction of regular shape could be observed, thanks to microstructural rearrangements. In contrast, treatments at lower temperature (800 °C) resulted in no porosity shape variation and an increase in both the mean and the standard deviation of porosity size, indicating both a more porous material and a more irregular distribution of the pores. 2) Macroscopically, the comparison with the AB state of longitudinal views underlines an evolution of the microstructure starting from the HTs at 800 °C for 20 min and 800 °C for 2 h, where the increase in treatment time led to a significantly less marked weld-like structure. Micrographs of samples heat treated at 1150 °C and HIP showed a completely recrystallized microstructure composed of equiaxed grains. The transversal view of the obtained microstructures in all conditions confirmed these observations. 3) Microscopically, the AB microstructure consisted of a fine cellular structure, where the γ phase was predominant, and small precipitates that seemed concentrated especially on the GB. The most significant differences were represented by the presence of γ+ε phase; in particular, ε phase was observed in the cellular structures with a major amount of intermetallic precipitations and/or carbides, which should lead in an increase of resistance and Young's modulus. The HT at 1150 °C led to a complete modification of the microstructure with the carbides being highly dissolved and resulting in very small precipitates. The presence of isotropy and equiaxed grains without differences of orientation and size also confirmed that a complete recrystallization occurred. The microstructure on samples heat treated at 1150 °C for 2 h showed the presence of γ+ε phases but the volume fraction of the ε phase drastically decreased with respect to HTs at 800 °C. The HT at 1150 °C for 6 h revealed no substantial changes in the microstructure, but it seemed that more diffusion could occur. The HIP-treated samples evolved in well-defined coarse grain structures, that is proof of complete recrystallization, and the isotropy was verified. The microstructure of HIP was homogenous with a prevalent presence of γ phase. The high temperatures of HT at 1150 °C and HIP treatments promoted the formation of annealing twin boundaries, in particular in the HT at 1150 °C specimens. The presence of a large fraction of annealing twins contributed to the increase in ductility of the material. The HT faster cooling generated a finer microstructure, more advisable for structural purposes, whereas for HIP, grain growth occurred and larger grains could be observed also in comparison with AB specimens. 4) For all cases, the values of yield stress $R_{p0.2}$ and ultimate tensile strength R_m satisfy the minimum requirements set by class 5 of ISO 22674 standard. When the material was heat treated at higher temperatures (i.e., 1150 °C and HIP), $R_{p0.2}$ slightly decreased, whereas R_m was almost unchanged after post-treatments. A remarkable increase in Young's modulus E and elongation at break A [%] could be also appreciated. The HT at lower temperatures showed a limited increase in R_m but a marked increase of the yield strength $R_{p0.2}$, increasing with holding time, and also showed a significant increase in elastic modulus E with a very limited change in elongation at break A [%]. 5) Considering wear behavior, the interpretation of results is not trivial due to the combination of several factors but HIP seems to be the best treatment under present testing conditions. In this case, the prevailing wear mechanism seemed to be adhesive wear. The HTs at 800 and 1150 °C for 2 h have similar COF and WRs, although the HTs at the 800 °C worn surface seemed more suitable to withstand wear, due to the presence of mainly adhesive wear. In addition, the morphology of worn surfaces presented smooth nondelaminated regions, which could be associated with oxidative wear contributing to the protection of sample surfaces. The samples treated at 1150 °C for 6 h had an uncharacteristic behavior with lower COF but higher WR. This sample had the most debris, making it plausible that the oxides debris remaining in the wear track were compact on the contact surface. Under this assumption, the compact oxide film could act as a protective layer on the

metal surface causing the COF reduction for this sample. In contrast, the higher specific WR value agrees with the plastic deformation, depth, and morphology of the worn track analyzed that is a consequence of an abrasive wear prevalence or of the presence of some local subsurface porosity. 6) Among all treatments, HIP seemed to provide the best balance between strength requirements, ductility, and wear resistance, thanks to the recrystallization processes and densification with consequent porosity reduction. 7) HT at 800 °C resulted in a significant increase in stiffness and yield strength but at the expense of ductility. Tribological performances could potentially be enhanced when compared with AB, because the same fine grain structure is maintained and HV is increased, but this advantage could be hindered in the presence of a significant level of porosity. 8) HT at a high temperature had a positive effect on ductility and, for the vacuum-assisted condition of the present work, may provide an interesting and less-expensive alternative to the HIP process. Tribological performances were lower in terms of WR, whereas the COFs were the lowest, but it is important to deepen with different test conditions.

Acknowledgements

The authors are grateful for the support given in the execution of heat treatments by TAV VACUUM FURNACES SpA, especially to Ing. Alessandro Fiorese.

Open Access Funding provided by Universita degli Studi di Brescia within the CRUI-CARE Agreement.

Conflict of Interest

The authors declare no conflict of interest.

Data Availability Statement

Research data are not shared.

Keywords

CoCrMo alloys, heat treatments, mechanical properties, selective laser melting, wear

Received: July 21, 2021
Revised: September 15, 2021
Published online:

[1] A. Takaichi, Suyalatu, T. Nakamoto, N. Joko, N. Nomura, Y. Tsutsumi, S. Migita, H. Doi, S. Kurosu, A. Chiba, N. Wakabayashi, Y. Igarashi, T. Hanawa, *J. Mech. Behav. Biomed. Mater.* **2013**, *21*, 67.
[2] T. Koutsoukis, S. Zinelis, G. Eliades, K. Al-Wazzan, M. A. Rifaiy, Y. S. Al Jabbari, *J. Prosthodont.* **2015**, *24*, 303.
[3] C. Song, Y. Yang, Y. Wang, D. Wang, J. Yu, *Int. J Adv. Manuf. Technol.* **2014**, *75*, 445.
[4] K. Hazlehurst, C. J. Wang, M. Stanford, *Mater. Des.* **2013**, *51*, 949.
[5] S. Limmahakhun, A. Oloyede, K. Sitthiseripratip, Y. Xiao, C. Yan, *Mater. Des.* **2017**, *114*, 633.
[6] D. Wei, Y. Koizumi, A. Chiba, K. Ueki, K. Ueda, T. Narushima, Tsutsumi, T. Yusuke, T. Hanawa, *Addit. Manuf.* **2018**, *24*, 103.
[7] S. Ayyıldız, E. H. Soylu, S. İde, S. Kılıç, C. Sipahi, B. Pişkin, H. Suat Gokce, *J. Adv. Prosthodont.* **2013**, *5*, 471.
[8] S. Y. Kim, S. Y. Shin, J. H. Lee, *J. Prosthet Dent.* **2018**, *119*, 1027.
[9] A. G. Demir, B. Previtali, *Mater. Des.* **2017**, *119*, 338.
[10] E. Ingham, J. Fisher, *Proc. Inst. Mech. Eng. Part H J. Eng. Med.* **2000**, *214*, 21.
[11] H. R. Kim, S. H. Jang, Y. K. Kim, J. S. Son, B. K. Min, K. H. Kim, T. Y. Kwon, *Mater* **2016**, *9*, 596.
[12] J. H. Wang, J. Ren, W. Liu, X. Y. Wu, M. X. Gao, P. K. Bai, *Mater* **2018**, *11*, 1546.
[13] M. Niinomi, C. J. Boehlert, *Advances in Metallic Biomaterials*, Vol. *3*, Springer Berlin Heidelberg, Berlin, Heidelberg **2015**.
[14] K. Asgar, F. A. Peyton, *J. Dent. Res.* **1961**, *40*, 73.
[15] Y. Bedolla-Gil, A. Juarez-Hernandez, A. Perez-Unzueta, E. Garcia-Sanchez, R. Mercado-Solis, M. A. L. Hernandez-Rodriguez, *Rev. Mex. FIS* **2009**, *55*, 1.
[16] D. L. Klarstrom, *ASM International*, Heat Treatment of Cobalt-Base Alloys By D.L. Klarstrom, Vol. *4E* (G. E. Totten), USA, **2006**, p. 625, https://doi.org/10.31399/asm.hb.v04e.a0006267.
[17] H. Minouei, M. H. Fathi, M. Meratin, H. Ghazvinizadeh, *Iran. J. Mater. Sci. Eng.* **2012**, *9*, 33.
[18] L. Hitzler, F. Alifui-Segbaya, P. Williams, B. Heine, M. Heitzmann, W. Hall, M. Merkel, A. Öchsner, *Adv. Mater. Sci. Eng.* **2018**, *2018*, 8213023.
[19] M. Zhang, Y. Yang, C. Song, Y. Bai, Z. Xiao, *Rapid Prototyp J.* **2018**, *24*, 1235.
[20] C. Song, M. Zhang, Y. Yang, D. Wang, Y. Jia-Kuo, *Mater. Sci. Eng., A* **2018**, *713*, 206.
[21] Y. Kajima, A. Takaichi, N. Kittikundecha, T. Nakamoto, T. Kimura, N. Nomura, A. Kawasaki, T. Hanawa, H. Takahashi, N. Wakabayashi, *Mater. Sci. Eng., A* **2018**, *726*, 21.
[22] M. Lorusso, *Frict. Lubr. Wear* **2019**, *1*, 1.
[23] B. AlMangour, J. Ming Yang, *Mater. Des.* **2016**, *110*, 914.
[24] B. AlMangour, D. Grzesiak, J. Cheng, Y. Ertas, *J. Mater. Process. Technol.* **2018**, *25*, 288.
[25] Y. Yang, X. Li, M. M. Khonsari, Y. Zhu, H. Yang, *Addit. Manuf.*, **2020**, *36*, 101583.
[26] H. Attar, K. G. Prashanth, A. K. Chaubey, M. Calin, L. C. Zhang, S. Scudino, J. Eckert, *Mater. Lett.*, **2015**, *142*, 38.
[27] F. Bartolomeu, M. Buciumeanu, E. Pinto, N. Alves, F. S. Silva, O. Carvalho, G. Miranda, *Trans. Nonferrous Met. Soc. China*, **2017**, *27*, 829.
[28] K. Duran, H. Mindivan, Ş.H. Atapek, M. Simov, T. Dikova, *presented in 19th International Metallurgy and Materials Congress IMMC 2018*, Istanbul (Turkey), October 2018.
[29] Ş. H. Atapek, T. Dikova, G. Aktaş, Ş. Polat, D. Dzhendov, D. Pavlova, M. Simov, *Mach. Technol. Mater.* **2016**, *10*, 61.
[30] K. M. Mantrala, M. Das, V. K. Balla, C. S. Rao, V. V. S. Kesava Rao, *Front. Mech. Eng.* **2015**, *1*, 1.
[31] C. D. Boley, S. A. Khairallah, A. M. Rubenchik, *Appl. Opt.* **2015**, *54*, 2477.
[32] C. Meier, R. W. Penny, Y. Zou, J. S. Gibbs, A. J. Hart, *Annu. Rev. Heat Transfer* **2017**, *20*, 241.
[33] H. Tan, C. K. Chua, K. F. Leong, C. M. Cheah, P. Cheang, M. S. Abu Bakar, S. W. Cha, *Biomaterials* **2003**, *24*, 3115.
[34] S. Bose, J. Darsel, H. L. Hosick, L. Yang, D. K. Sarkar, *J. Mater. Sci.* **2002**, *13*, 23.
[35] S. J. Kalitaa, S. Bose, L. H. Howard, A. Bandyopadhyay, *Mater. Sci. Eng.C* **2003**, *23*, 611.
[36] G. T. M. Chu, A. G. Brady, W. Miao, J. W. Halloran, S. J. Hollister, D. Brei, in *Proc. the MRS Fall Meeting Symp. V: Solid Freefrom and Additive Fabrication*, Vol. *542*, Boston, USA **1998**, p. 119.

[37] Ö. İlkgün, *M.Sc. Thesis*, *Middle East Technical University, (Turkey)*, **2005**.
[38] E. Malekipour, H. El-Mounayri, *Int. J. Adv. Manuf. Technol.* **2017**, *95*, 527.
[39] Y. Okazaki, *Mater. Trans.* **2008**, *49*, 817.
[40] N. Chawla, X. Deng, *Mater. Sci. Eng., A* **2005**, *390*, 98.
[41] K. P. Monroy, J. Delgado, L. Sereno, J. Ciurana, N. J. Hendrichs, *Met. Mater. Int.* **2014**, *20*, 873.
[42] I. Yadroitsev, M. Pavlov, Ph. Bertand, I. Smurov, *presented to 14th European Meeting Prototyping & Rapid Manufacturing*, Paris, June 2009.
[43] B. AlMangour, M. Luqman, D. Grzesiak, H. Al-Harbi, F. Ijaz, *Mater. Sci. Eng., A* **2020**, *792*, 139456.
[44] S. M. J. Razavi, A. Avanzini, G. Cornacchia, L. Giorleo, F. Berto, *2021 Int. J.Fatigue* **2021**, *142*, 105926.
[45] A. Majeed, Y. Zhang, J. Lv, T. Peng, Z. Atta, A. Ahmed, *Comput. Ind. Eng.* **2020**, 106194.
[46] S. H. Lee, E. Takahashi, N. Nomura, A. Chiba, *Mater. Trans.* **2005**, *46*, 1790.
[47] K. G. Prashanth, J. Eckert, *J. Alloy. Compd.* **2017**, *707*, 27.
[48] P. Huang, H. F. Lopez, *Mater. Lett.* **1999**, *39*, 249.
[49] Y. Lu, S. Wu, Y. Gan, J. Li, C. Zhao, D. Zhuo, J. Lin, *Mater. Sci. Eng., C* **2015**, *49*, 517.
[50] Y. S. Hedberg, B. Qian, Z. Shen, S. Virtanen, I. O. Wallinder, *Dent. Mater.* **2014**, *30*, 525.
[51] K. Darvish, Z. W. Chen, M. A. L. Phan, T. Pasang, *Mater. Charact.* **2018**, *135*, 83.
[52] R. Turrubiates-Estrada, A. Salinas-Rodriguez, H. F. Lopez, *J. Mater. Sci.* **2011**, *46*, 254.
[53] K. C. Li, D. J. Prior, J. N. Waddell, M. V. Swain, *J. Mater. Res.* **2015**, *30*, 2188.
[54] Y. Lu, S. Wu, Y. Gan, S. Zhang, S. Guo, J. Lin, J. Lin, *J. Mech. Behav. Biomed. Mater.* **2016**, *55*, 179.
[55] J. Haan, M. Asseln, M. Zivcec, J. Eschweiler, R. Radermacher, C. Broeckmann, *Powder Metall.* **2015**, *58*, 161.
[56] Y. P. Li, Y. Koizumi, A. Chiba, *Mater. Sci. Eng., A* **2016**, *668* 86.
[57] F. C. Liu, X. Lin, G. L. Yang, M. H. Song, J. Chen, W. D. Huang, *Opt. Laser Technol.* **2011**, *43*, 208.
[58] I. Toda-Caraballo, J. Chao, L. E. Lindgren, C. Capdevila, *Scr. Mater.* **2010**, *62*, 41.
[59] W. M. Tucho, P. Cuvillier, A. Sjolyst-Kverneland, V. Hansen, *Mater. Sci. Eng., A* **2017**, *689*, 220.
[60] A. Selldén, *Degree Thesis Evaluation of Heat Treatments for the Nickel-Based Superalloy Haynes® 282® Manufactured by Selective Laser Melting : A Study Based on Microstructural Examinations and Mechanical Testing, Linköping University (Sweden)*, **2017**.
[61] ISO UNI EN 22674 1:2004, *Dentistry—Metallic Materials for Fixed and Removable Restorations and Appliances*, International Organization for Standardization (ISO), Geneva **2004**.
[62] C. A. Lewinsohn, *Mater. Manuf. Process.* **2000**, *15*, 775.
[63] K. Yamanaka, M. Mori, A. Chiba, *J. Mech. Behv. Biomed. Mater.* **2014**, *29*, 417.
[64] G. Straffelini, *Attrito e usura. Metodologie di progettazione e controllo*, Tecniche Nuove, Italia **2005**.
[65] Y. Chen, Y. Li, S. Kurosu, K. Yamanaka, N. Tang, Y. Koizumi, A. Chiba, *Wear* **2014**, *310*, 51.
[66] M. A. Wimmer, J. Loos, R. Nassutt, M. Heitkemper, A. Fischer, *Wear* **2001**, *250–251*, 129.
[67] W. Q. Toh, X. Tan, A. Bhowmik, E. Liu, S. B. Tor, *Mater.* **2017**, *11*, 30.
[68] W. Quan Toh, Z. Sun, X. Tan, E. Liu, S. B. Tor, C. K. Chua, in *2nd Int. Conf. Progress in Additive Manufacturing*, Research Publishing, Singapore **2016**, p. 342.
[69] X. P. Tan, P. Wang, Y. Kok, W. Q. Toh, Z. Sun, S. M. L. Nai, M. Descoins, D. Mangelinck, E. Liu, S. B. Tor, *Scr. Mater.* **2018**, *143*, 117.
[70] C. Trevisiol, A. Jourani, S. Bouvier, *Tribol. Int.* **2017**, *113*, 411.
[71] Y. Zhang, A. Jourani, *Mater.* **2021**, *14*, 2964.
[72] R. Varano, J. D. Bobyn, J. B. Medley, S. Yue, *J. Biomed. Mater. Res. B Appl. Biomater.* **2006**, *76*, 281.
[73] J. Mølgaard, *Wear* **1976**, *40*, 277.
[74] H. So, D. Yu, C. Chuang, *Wear* **2002**, *253*, 1004.
[75] S. Q. Wang, M. X. Wei, Y. T. Zhao, *Wear* **2010**, *269*, 424.
[76] M. X. Wei, K. M. Chen, S. Q. Wang, X. H. Cui, *Tribol. Lett.* **2011**, *42*, 1.
[77] Q. Zhang, K. Chen, L. Wang, X. Cui, S. Wang, *Tribol. Int.* **2013**, *61*, 214.